Theses and Dissertations	1. Thesis and Dissertation Collection, all items

2019-03

TETHERED SPACECRAFT SYSTEMS FOR ACTIVE DEBRIS REMOVAL

Shapiro, Jessica

Monterey, CA; Naval Postgraduate School

http://hdl.handle.net/10945/62294

NAVAL POSTGRADUATE SCHOOL

MONTEREY, CALIFORNIA

THESIS

TETHERED SPACECRAFT SYSTEMS FOR ACTIVE DEBRIS REMOVAL

by

Jessica Shapiro

March 2019

| Thesis Advisor: | Marcello Romano |
| Co-Advisor: | Gregory J. Byrne |

Approved for public release. Distribution is unlimited.

THIS PAGE INTENTIONALLY LEFT BLANK

REPORT DOCUMENTATION PAGE		*Form Approved OMB No. 0704-0188*

Public reporting burden for this collection of information is estimated to average 1 hour per response, including the time for reviewing instruction, searching existing data sources, gathering and maintaining the data needed, and completing and reviewing the collection of information. Send comments regarding this burden estimate or any other aspect of this collection of information, including suggestions for reducing this burden, to Washington headquarters Services, Directorate for Information Operations and Reports, 1215 Jefferson Davis Highway, Suite 1204, Arlington, VA 22202-4302, and to the Office of Management and Budget, Paperwork Reduction Project (0704-0188) Washington, DC 20503.

1. AGENCY USE ONLY *(Leave blank)*	2. REPORT DATE March 2019	3. REPORT TYPE AND DATES COVERED Master's thesis	
4. TITLE AND SUBTITLE TETHERED SPACECRAFT SYSTEMS FOR ACTIVE DEBRIS REMOVAL		5. FUNDING NUMBERS	
6. AUTHOR(S) Jessica Shapiro			
7. PERFORMING ORGANIZATION NAME(S) AND ADDRESS(ES) Naval Postgraduate School Monterey, CA 93943-5000		8. PERFORMING ORGANIZATION REPORT NUMBER	
9. SPONSORING / MONITORING AGENCY NAME(S) AND ADDRESS(ES) N/A		10. SPONSORING / MONITORING AGENCY REPORT NUMBER	

11. SUPPLEMENTARY NOTES The views expressed in this thesis are those of the author and do not reflect the official policy or position of the Department of Defense or the U.S. Government.

12a. DISTRIBUTION / AVAILABILITY STATEMENT Approved for public release. Distribution is unlimited.	12b. DISTRIBUTION CODE A

13. ABSTRACT (maximum 200 words)

Orbital debris will increase dramatically unless active debris removal methods are implemented. Tethered methods of active debris removal present an intriguing solution that should be investigated and the benefits compared to other researched methods of active debris removal. This study consists of applications of tethered space systems and active debris removal methods with a focus on tether-based momentum exchange systems in an effort to determine if a tethered propellantless debris removal solution is a viable one. The debris will be assumed to have been captured, with the tether attached to the center of mass of both the debris and the removal vehicle. The debris analyzed has simplified characteristics based on Hubble Space Telescope. The results of this study, conducted primarily using MATLAB and Simulink numerical integration methods, explore the dynamics of tethered satellite systems and compare the results of different removal methods, including the addition of a drag sail via a long tether, tethered momentum exchange orbital transfers, and propulsive orbital transfers. The momentum exchange model explores effects of tether length and spin rate on the momentum exchange orbital transfer.

14. SUBJECT TERMS tether space system, active debris removal, momentum exchange, orbital transfer			15. NUMBER OF PAGES 91
			16. PRICE CODE
17. SECURITY CLASSIFICATION OF REPORT Unclassified	18. SECURITY CLASSIFICATION OF THIS PAGE Unclassified	19. SECURITY CLASSIFICATION OF ABSTRACT Unclassified	20. LIMITATION OF ABSTRACT UU

NSN 7540-01-280-5500

Standard Form 298 (Rev. 2-89)
Prescribed by ANSI Std. 239-18

THIS PAGE INTENTIONALLY LEFT BLANK

TETHERED SPACECRAFT SYSTEMS FOR ACTIVE DEBRIS REMOVAL

Jessica Shapiro
Lieutenant, United States Navy
BS, U.S. Naval Academy, 2012

Submitted in partial fulfillment of the
requirements for the degree of

MASTER OF SCIENCE IN ASTRONAUTICAL ENGINEERING

from the

**NAVAL POSTGRADUATE SCHOOL
March 2019**

Approved by: Marcello Romano
        Advisor

        Gregory J. Byrne
        Co-Advisor

        Garth V. Hobson
        Chair, Department of Mechanical and Aerospace Engineering

THIS PAGE INTENTIONALLY LEFT BLANK

ABSTRACT

Orbital debris will increase dramatically unless active debris removal methods are implemented. Tethered methods of active debris removal present an intriguing solution that should be investigated and the benefits compared to other researched methods of active debris removal. This study consists of applications of tethered space systems and active debris removal methods with a focus on tether-based momentum exchange systems in an effort to determine if a tethered propellantless debris removal solution is a viable one. The debris will be assumed to have been captured, with the tether attached to the center of mass of both the debris and the removal vehicle. The debris analyzed has simplified characteristics based on Hubble Space Telescope. The results of this study, conducted primarily using MATLAB and Simulink numerical integration methods, explore the dynamics of tethered satellite systems and compare the results of different removal methods, including the addition of a drag sail via a long tether, tethered momentum exchange orbital transfers, and propulsive orbital transfers. The momentum exchange model explores effects of tether length and spin rate on the momentum exchange orbital transfer.

THIS PAGE INTENTIONALLY LEFT BLANK

Table of Contents

List of Figures

List of Tables

THIS PAGE INTENTIONALLY LEFT BLANK

List of Acronyms and Abbreviations

ADR   Active Debris Removal

BVP   Boundary Value Problem

CNES   National Centre for Space Studies

CW   Clohessy-Wiltshire

DARPA   Defense Advanced Research Projects Agency

DCM   Direction Cosine Matrix

DoD   Department of Defense

ECEF   Earth Centered-Earth Fixed

ECI   Earth Centered Inertial

EDT   Electro Dynamic Tether

HST   Hubble Space Telescope

IADC   Inter-Agency Space Debris Coordination Committee

ISAS   Institute of Space and Astronautical Sciences

ISS   International Space Station

LAE   Liquid Apogee Engine

LEO   Low Earth Orbit

LVLH   Local Vertical Local Horizontal

NASA   National Aeronautics and Space Administration

NPS   Naval Postgraduate School

ODPO   Orbital Debris Program Office

PMD   Post Mission Disposal

RAAN   Right Ascension of the Ascending Node

STELA   Semi-analytic Tool for End of Life Analysis

SV   Service Vehicle

TSS   Tethered Satellite System

USN   U.S. Navy

USG   United States Government

Acknowledgments

I would like to thank my advisor, Dr. Marcello Romano, and my second reader, Dr. Gregory Byrne, for their guidance and support. I would also like to thank Dr. Kevin Viner for being a voice of reason, a sounding board, troubleshooter, and sanity checker. In addition, I would like to express my gratitude to my friends and cohort, especially my fellow Spacecraft Robotics Laboratory members Katrina and Justin, without whom none of this would have been possible, and finally, I would like to thank all the great faculty and staff of the Space Systems Academic Group.

THIS PAGE INTENTIONALLY LEFT BLANK

CHAPTER 1:
Introduction

One of the major issues facing future operations in space is the rapidly increasing population of orbital debris, or space junk in Earth's orbit. Orbital debris is composed of defunct human-made objects over a wide range of sizes; objects larger than about 10 cm are trackable and cataloged in the U.S. Space Surveillance Catalog. Active Debris Removal (ADR) methods have been proposed, and unless ADR is implemented, the space junk population will increase dramatically, presenting hazards to current and future space missions. Tethered methods of active debris removal present an intriguing solution that should be investigated and the benefits compared to other methods of active debris removal.

This study consists of surveys of tethered space systems and active debris removal methods with a focus on tethered space tugs and momentum-exchange systems. The debris is assumed to have been captured, with the tether attached to the center of mass of both the debris and the removal vehicle. The debris analyzed is an intact spacecraft with simplified characteristics loosely based on Hubble Space Telescope (HST).

This study compares the results of different removal methods, including the addition of a drag sail to the debris, the addition of a drag sail mounted on a spacecraft at a lower orbit, connected via a long tether, tethered momentum-exchange orbital transfers, and propulsive orbital transfers. The tethered-sail system model offers a parametric comparison exploring how changes in tether length and orbital altitude differences affect deorbit time. It is assumed that the drag sail area remains constant and the drag sail system is attitude-controlled to utilize the maximum drag area. The momentum-exchange model explores effects of tether length on the momentum-exchange orbital transfer. By comparison of propellantless tethered deorbit solutions to more conventional propulsive methods, this thesis determines that tethered ADR solutions are feasible and can be more economical than other proposed ADR methods. This chapter begins by reviewing orbital debris mitigation practices, followed by the current state of active debris removal. As this thesis is specifically focused on investigation of tethered ADR systems, Section 1.2.1 also includes a survey of tethered space systems.

1.1 Orbital Debris

There are currently more than 20,000 known, monitored objects larger than 10 cm that present debris hazards in the Low Earth Orbit (LEO) environment (up to 2000 km). The debris includes non-operational spacecraft; derelict launch vehicle stages; mission-related debris such as sensor covers, engine covers, straps, etc., which were typically considered expendable parts in missions from the '60s and '70s; or fragmentation debris, which can be due to anomalous events, explosions, or collisions [1]. The debris population fluctuates as a function of solar flux (and thereby, atmospheric density) and of major debris generating events, such as the 2007 Fengyun-1C Chinese anti-satellite missile test and the 2009 Cosmos and Iridium collision. Atmospheric drag is a function of density, so as atmospheric density fluctuates with solar activity, the atmospheric drag force increases, resulting in faster deorbit rates.

Debris from events such as these increased the hazard to space assets and further endangers human spaceflight missions. For example, the International Space Station (ISS) is required to maneuver if there is a debris collision risk greater than 1 in 100,000 and mission objectives would not be compromised, requiring propellant usage. If the risk of collision is too great, and ISS is unable to maneuver, the crew must board the Soyuz spacecraft to prepare to undock [1]. These risks are currently manageable, but as the debris population increases, so will the risk to space assets. Additionally, as the amount of debris grows, shielding solutions will have to be implemented on future launches [1]. Moreover, constellations of small satellites are rapidly becoming a popular option for aerospace companies, but as these satellites become inoperable with age, they will add to the orbital debris pollution problem in LEO. Large constellations will potentially add thousands of small satellites to an already congested environment. In order to assess the impact to the LEO environment, where we do most of our satellite business, a recent study on large constellations was conducted by the National Aeronautics and Space Administration (NASA) Orbital Debris Program Office (ODPO). The study showed that even with a best-case scenario of 99 percent success rate of post-mission disposal of constellation satellites within five years of conclusion of their mission (in addition to post-mission disposal of normal LEO satellites), the implementation of large constellations would still add to the debris population by 22 percent over the next 200 years [2].

Models have shown that the debris population in LEO will continue to increase in a runaway

nonlinear fashion, even if all future launches are stopped, due to collisions between orbiting objects, a phenomenon known as the Kessler Syndrome, identified by NASA in 1978 [3]. This study utilized a modeling tool called the LEO-to-GEO Environment Debris (LEGEND) model to simulate and predict debris populations in LEO. This model uses a deterministic approach to evaluate debris populations in a simulated environment based on historical data and a comprehensive NASA ODPO internal database. The debris population projection, shown in Figure 1.1 was based on the average results of 100 Monte Carlo simulations using this tool, assuming no future launches [3].
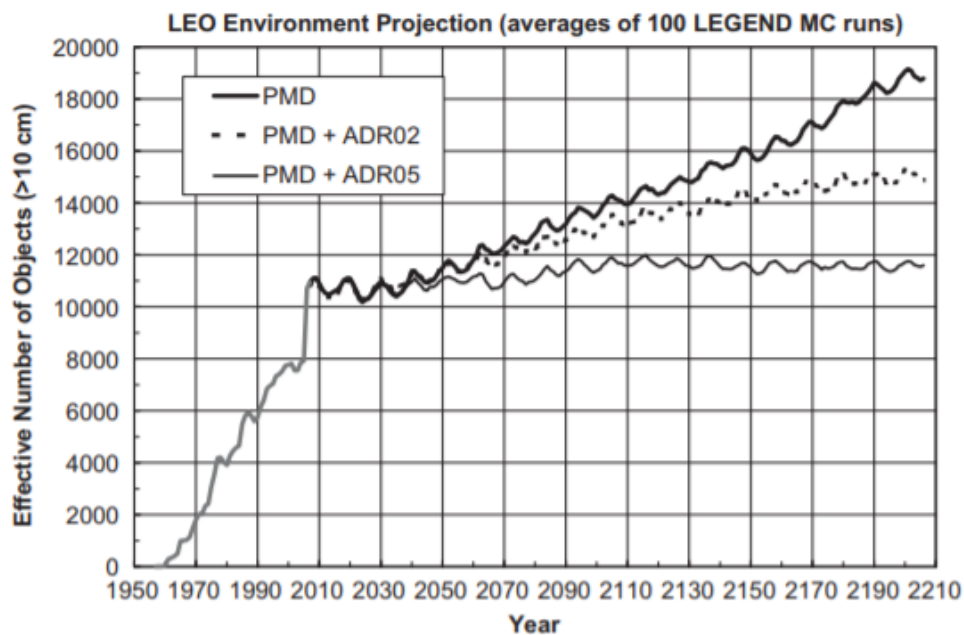
Figure 1.1. 200-Year Projection of Debris Population. Source: [3].

As the debris population increases, the risk of collision increases, and further collisions and explosions create new debris in an endless positive feedback loop. During a technical seminar in 2011, NASA's chief scientist for orbital debris, J.-C. Liou [4], reported that, as the debris population increases, more frequent conjunction assessments will be needed; more collision avoidance maneuvers will need to be made; more debris impact shields will be needed, which adds more mass requirements to future systems and limits launch capability; and the risk for potential critical failures due to collisions or explosions will increase. Likewise, projections show that without post-mission disposal or other mitigation, over the next 200 years, the number of debris objects in LEO experiences a 330 percent population

3

increase with dramatic catastrophic collision potential [2].

A 2009 baseline study [2] by NASA's ODPO determined that even if all future launches were suspended, and even if post-mission disposal of re-entry within 25 years, in accordance with debris mitigation policies, was 90 percent successful, the debris population would still increase by 75 percent over the next 200 years. However, this same study determined that by implementing an ADR program, the debris population is in fact manageable; by removing at least five objects a year, the debris population can be held relatively constant. Currently, though, ADR is not a commonly practiced solution because it is technically difficult and expensive. Further complicating the issue is that international treaties prohibit the removal of space objects by anyone other than their owner, so there are political factors such as ownership and liability to consider [5].

1.1.1 Orbital Debris Mitigation

In an effort to limit future debris creation events, many policies have been implemented by the spacefaring nations. The Inter-Agency Space Debris Coordination Committee (IADC) is an international governmental forum for the worldwide coordination of activities related to the issues of man-made and natural debris in space. Current IADC Orbital Debris Mitigation Policy states that upon completion of its mission, a satellite either shall reenter the atmosphere within 25 years, or shall be removed to a storage orbit during a process called Post Mission Disposal (PMD). NASA refers to this policy as "design for demise" whereby all current launches must include some end-of-life disposal methods to adhere to this policy and reduce the risk of casualty [1]. Disposal methods include the use of drag enhancement devices, or including the propellant required for propulsive deorbit, or transfer to a graveyard orbit in the propellant budget. Drag enhancement involves increasing the cross-sectional area of the system to exploit atmospheric drag to increase the rate of orbital decay. The method of adding a drag enhancement device to a tethered system will be investigated in Chapter 4. For satellites without maneuvering capabilities, mission orbits are often simply chosen in which natural atmospheric drag will deorbit the object within 25 years. This straightforward approach is popular with many of the newer CubeSat experiments [6]. Additionally, passivation is required upon mission completion to deplete all on-board sources of energy. This practice minimizes the impact of accidental collision or reduces risk of explosions from stored fuel on-board spacecraft or upper stages [7].

However, as discussed previously, PMD alone is insufficient to protect the space environment. Additional policy changes have been suggested to impose taxation to fund cleanup efforts and limit future launches. There is, however, concern that this would limit the accessibility of space and is unfair to smaller space agencies as most of debris is from three major players (United States, Russia, and China) [1]. While PMD offers a solution to future debris remediation, ADR methods can be applied to persistent non-compliant debris that have been a high risk to further polluting the LEO environment for many years [6]. Due to the cost and complexities involved in ADR, the debris candidates for ADR must be prioritized and selected carefully. The removal criterion is determined by debris mass and its collision probability over time. Once an object has been selected for removal, it must be removed quickly to mitigate its collision risk [3].

1.1.2 Active Debris Removal Concepts

In a 2013 internal report, NASA identified several major strategies for ADR methods for large debris removal. In particular, they reviewed drag enhancement devices such as drag sails and inflatables, lasers, Electro Dynamic Tether (EDT) space tugs, the Geosynchronous Large Debris Deorbiter (GLiDeR) concept, Frozen mist, ballistic intercept, tungsten dust, laser collision avoidance, and the ion beam shepherd [8].

In September 2018, Surrey Satellite's RemoveDebris payload demonstrated successful debris capture with its on-board net technology in the first successful demonstration of ADR technology in human history [9]. This payload contains additional experiments for vision-based navigation for non-cooperative rendezvous, a harpoon debris capture experiment with a 25 m tether, and a drag sail demonstration [10].

Other upcoming ADR missions include ESA's Clean Space initiative that, is developing the e.deorbit satellite to remove a large piece of debris, and the CleanSat program, that aims to develop technologies to ensure that future satellites are able to comply with debris regulations [11]. E.deorbit is planned to launch in 2023. Its mission is to capture a large piece of ESA-owned debris in the 800-1000 km altitude range, in a near polar orbit and is considering net capture, or robotic arms with grippers to capture its target [12]. The ultimate deorbit method considered resembles a space tug. Space tugs are debris removal vehicles that rendezvous and grapple a debris object to relocate it into a disposal orbit,

5

usually via propulsive means.

CleanSpaceOne is a proposed ADR technology demonstration to capture the Swiss-owned SwissCube [11]. Challenges for this demonstration include detection and capture, due to SwissCube's small size and high tumble rate. As of this year, this project is still in the funding consolidation phase [13].

The GLiDeR concept proposes using active charge emissions and directed charged particles to increase the absolute electric potential of a debris object and deposit it into a graveyard orbit. This method is unique in that debris objects can be moved into its disposal orbit without requiring any physical contact between the GLiDeR and the debris [14].

Lasers are also being investigated as a debris removal method. A laser could potentially vaporize a portion of the debris, generating a thrust which causes the debris to alter its orbit [1]. There is, however concern that this method may generate small debris particles, which would potentially interfere with operational satellites. Sweeper satellites could be used in conjunction with this method to remove the small debris particles [6].

The NASA 2013 report [8] concluded that drag enhancement devices, space tugs, and electrodynamic tethers were the most viable large debris removal concepts based on mission suitability, technology readiness, schedule, risks and cost. This drives the motivation of this study for investigation into these methods in particular [8]. A tethered ADR system would reduce the fuel requirement for a deorbit system and can be completely passive. Tethered space tug systems are being considered due to the advantages of being lightweight, flexible, and with simple controller design. Several companies are developing electrodynamic terminator tether tape technologies for SmallSats and CubeSats. A conductive tether induces an electric potential generated by its motion through the earth's magnetic field; the resultant Lorentz force slowly deorbits the object [1]. Patents have been developed by Researchers at the Universidad Carlos III de Madrid for power generation via tethers as a satellite lowers in altitude, transforming orbital energy into electromagnetic energy via passive exploitation of Lorentz drag to remove inactive satellites [15].

Additionally, momentum tethers are an option considered by NASA [1]. Momentum tethers use the rotation of a debris removal vehicle to generate momentum and remove the object to a lower orbit once the tether is severed on the principle of dynamic release. This method

6

in particular will be investigated thoroughly in Chapter 5. A momentum tether scenario proposed by NASA involves attaching a non-conductive tether to a piece of orbital debris, generating momentum, then severing the tether to use the generated momentum to swing the object out of orbit. This method may effectively deorbit large masses, which are the greatest concern for collision risks [1]. A momentum exchange tether system is also a solution worth investigation because these systems can also be used for propellantless formation flight and stationkeeping. The "TAMU sling sat sweeper" concept proposes using inelastic collisions to capture debris and using a change in angular rate to appropriately expel the debris with the desired conditions. Additionally, the momentum exchange from this maneuver can be used to assist in orbital transfer to a subsequent debris for capture, minimizing the necessary propellant used by the sweeper vehicle [16].

The most cost effective space tugs mission would be able to service multiple debris objects [6]. There are many technical challenges to this method. Rendezvousing with and grappling a tumbling debris object requires very sophisticated guidance and control, and the grappling mechanism must be robust enough to accommodate all sorts of extended structures and odd shapes [6]. The European company Airbus is also developing a space tug for on-orbit maintenance and debris removal. Airbus developed the debris capture net that was demonstrated on the removeDebris mission, as well as the harpoon capture system, and the visual based navigation system that will be demonstrated in the following stages of the mission [9].

In 2017, Defense Advanced Research Projects Agency (DARPA) awarded Space Systems Loral (SSL) the contract for their Robotic Servicing of Geosynchronous Satellites (RSGS) program, which includes relocation and other orbital maneuvers. This program will also develop many of the technologies and techniques that can be applied to ADR. SSL's RSGS payload is anticipated to launch in 2021 [17].

1.2 Tethered Spacecraft Systems

Tethered ADR methods are some of the primary researched methods by major space industry players because the advantages of implementing tethers in space have been apparent since before the dawn of the space program. Many applications of tethered space systems have been studied and explored, including propellantless formation flying, momentum

exchange maneuvers, debris removal and towing, aerobraking for deorbiting maneuvers, power generation or propulsion via electrodynamic tethers, generating microgravity for on-orbit refueling, and, upper atmosphere exploration [18].

1.2.1 Review of Tethered Space Missions

The first concept of a tethered space system was developed in 1895 by Russian scientist Konstantin Tsiolkovsky when he conceived the idea for a "space elevator" [19]. This was followed by Yuri Artsutanov's concept in 1960 of using a geostationary satellite as a base to deploy a structure toward earth using a counterweight to maintain a stationary center of gravity [20]. In 1966, Gemini-11 conducted a 30 m tethered experiment to generate .0005g of artificial gravity via the spin between the capsule and the target vehicle [21]. The following mission, Gemini-12, demonstrated tethered station-keeping with the Agena target vehicle and gravity-gradient vertical stability [22].

The early 1980s produced several joint experiments between NASA and Institute of Space and Astronautical Sciences (ISAS). TPE-1, TPE-2, Charge-1, Charge-2, were all suborbital sounding rocket tests with electrodynamic tethers to study upper atmospheric conditions. Charge-2 utilized control thrusters to maintain tether tension. OEDIPUS-A and C were sounding rocket experiments with NASA and Canada to provide data about the ionosphere [22].

TSS-1 was a joint NASA/Italian Space Agency (ISA) mission launched in 1992 on STS-46 and deployed 268m above the orbiter, demonstrating the feasibility of a gravity gradient stabilized system [23], TSS-1R was the follow-on mission flown on STS-75 in 1996. The goal was a 20.7 km tether deployed from the Space Shuttle Columbia for space plasma physics experiments [24]. The tether managed to deploy to 19.6 km, but severed due to electric arcing within the tether, inadvertently demonstrating momentum exchange on both the shuttle and the deployed satellite as both were moved into new, elliptical orbits [22]. The Small Expendable Deployer System Missions (SEDS) used active braking and feedback control for tether deployment and to limit residual swing and proved several stability concepts [22]. The Plasma Motor Generator (PMG) in 1996 was a conducting tether that proved that orbital energy could be converted into electrical energy and the ability to use electrostatic tethers as an orbit boosting device, vice propellant. [20]. Tether Physics and Survivability Spacecraft (TiPS) employed a larger diameter tether to ensure

resilience to severing and studied long term tether dynamics and remained in orbit for over 10 years. [25]. Most of the failures for these missions are due to deployment problems, or tether severing due to manufacturing faults, parent satellite safety considerations, or cut due to impact. A summary of tethered missions is provided in Table 1.1.

1.2.2 Tethered Spacecraft Dynamics

In this thesis, the tethered debris removal system was modeled as a dumbbell spacecraft system. The dumbbell spacecraft system consists of two satellites connected by a rigid, massless tether. This system can be described as a rigid body, exhibiting a pendular motion about the system's center of mass. Coupling effects are studied by using the radial motion, orbital motion, and in-plane libration motion [27]. Libration refers to the perceived oscillation of orbiting bodies relative to each other (i.e., the oscillating motion about a point of equilibrium [28]). The dynamics of this system will be explored in later chapters.

1.3 Research Objectives and Thesis Organization

The goal of this thesis is to develop a comparison of two tethered methods of ADR: a space tug with the addition of a drag device, and a momentum exchange tethered system. This will be done via parametric analyses and observation of the dynamical model of each method. These methods will be compared to an optimized propulsive deorbit method.

This thesis is divided into seven chapters. Chapter 2 provides a review of applicable orbital mechanics concepts, Chapter 3 offers a baseline analysis on the orbital lifetime of the debris object candidate for ADR, Chapter 4 presents a derivation of the relative motion equations of a tethered satellite system, Chapter 5 explores momentum exchange ADR methods, and Chapter 6 explores optimization methods for propulsive deorbit. Both Chapters 5 and 6 utilize models developed in MATLAB and Simulink. Finally, Chapter 7 offers a summary, conclusions, and recommendations for areas of future research into tethered ADR. The analyses presented in these chapters show that propulsive deorbit methods can be effective and reliable, but extremely costly and inefficient; therefore, a tethered, propellantless, deorbit mission can not only feasibly attain the desired re-entry conditions, but can do so in a more economical manner, across wider variety of debris objects, making it a potentially preferred ADR solution.

Table 1.1. Summary of Space Tether Missions. Adapted from [20] and [26].

Name	Year	Orbit	Length	Agency	Comments
Gemini-11	1966	LEO	30 m	NASA	Spin stable 0.15 rpm
Gemini-12	1966	LEO	30 m	NASA	Local vertical, stable swing
TPE-1	1980	Suborbital	500 m	NASA/ISAS	EDT Partially deployed 38m
TPE-2	1981	Suborbital	500m	NASA/ISAS	Partially deployed 65 m
Charge-1	1983	Suborbital	418m	NASA/ISAS	Fully deployed
Charge-2	1984	Suborbital	426m	NASA/ISAS	Fully deployed
Oedipus-A	1989	Suborbital	958m	CSA/NASA	Spin stable @ 7 Hz, magnetic field aligned
Charge-2B	1992	Suborbital	500m	NASA	Fully deployed
TSS-1	1992	LEO	260m	NASA/ISA	Partially deployed, retrieved
SEDS-1	1993	LEO	20 km	NASA	Downward fully deployed, swing, and cut
PMG	1993	LEO	500m	NASA	Upward deployed
SEDS-2	1994	LEO	20km	NASA	Fully deployed, local vertical, stable
Oedipus-C	1995	Suborbital	1170 m	CSA/NASA	Spin stable @ 5 rpm, magnetic field aligned
TSS-1R	1996	LEO	19.6 km	NASA/ISA	Close to full deployment, severed by arcing
TiPS	1996	LEO	4 km	NRO/NRL	Long-life tether on-orbit (survived 12 years)
ATEx	1999	LEO	6 km	NRL	Partially deployed (22 m)
ProSEDS	1999	LEO	15 km	NASA	Hardware build but not flown
DTUsat-1	2003	LEO	450 m	TUD	Nano-Satellite failed to work in space
MAST	2007	LEO	1 km	NASA	Tether failed to deploy
YES2	2007	LEO	30 km	ESA	Fully deployed
Cute-1.7+APDII	2008	LEO	10 m	Tokyo Tech, Japan	Cube-Satellite worked, Tether failed to deploy
STARS	2009	LEO	10 km	Kagawa U, Japan	Space tethered robot mission, tether not fully deployed
T-Rex	2010	Suborbital	300 m	JAXA	Tether deployed, current not measured
STARS-II	2014	LEO	300 m	JAXA	Electrodynamic tether deployment not confirmed
KITE	2016	LEO	700 m	JAXA	Deployment failure
STARS-C	2016	LEO	100 m	JAXA	Tether deployment not confirmed
removeDebris	2018	LEO	25 m	ESA	Harpoon debris capture demo

CHAPTER 2:
Astrodynamics

To evaluate the viability of tethered ADR, it will be necessary to draw upon a number of concepts in the field of orbital mechanics. This section provides an overview of several of these concepts and offers a preliminary analysis of their applicability to tethered ADR.

2.1 Classical Orbital Elements

The Classical Orbital Elements, shown in Figure 2.1, are the parameters by which the orbit of any spacecraft, such as an ADR system, is described, shown below [28].

$$œ = \{a, e, i, \Omega, \omega, \nu\}$$

a is the semi-major axis of the elliptical orbital plane and describes the size of the orbit. The eccentricity, e, describes the shape of the orbit and $0 \leq e < 1$ for all closed orbits. In vector form, the eccentricity vector points from apogee to perigee. i is the inclination, or the angle from the equatorial plane to the orbital plane. The right ascension of the ascending node, Ω, refers to the angle from the geocentric axis pointing to the first point of Aries, shown in Figure 2.1 as the X axis, to the node line, which is the intersection of the orbital plane and the equatorial plane [29]. The ascending node is referred to as such because it is the point on the orbit where the object moves north through the plane [30]. ω is the argument of perigee and refers to the angle between the line pointing to the ascending node and the perigee direction of the satellite motion. In this thesis, as all orbits described are Earth orbits, the terms periapsis and perigee may be used interchangeably. The true anomaly ν describes the position of the object along its orbital path described as the angle between the direction of periapsis and the current position. The inertial position and velocity of a spacecraft depend on time and the classical orbital elements.
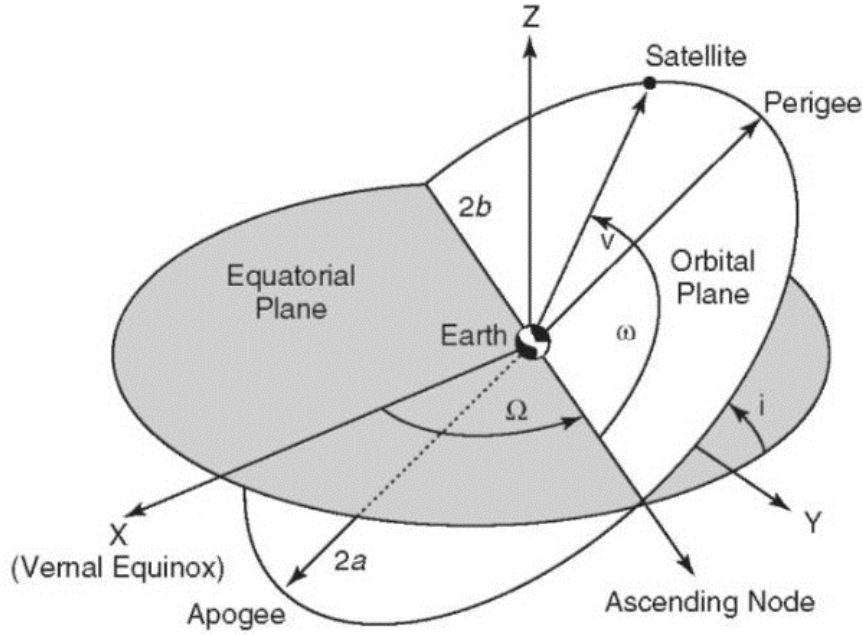
Figure 2.1. Classical Orbital Elements. Source: [29].

2.2   Two-Body Problem

To accurately describe the dynamics of a tethered ADR system, the motion of the system as a whole must be considered in its orbit around Earth. This is given by the classical Keplerian simplified two-body problem. The two-body problem states:

$$\ddot{\mathbf{r}} = \frac{-\mu}{r^3}\mathbf{r} \tag{2.1}$$

for any satellite position $\mathbf{r}$, where μ is the standard gravitational parameter used in celestial mechanics, and $\mathbf{r} = [X, Y, Z]^T$, the satellite's position vector in the Earth Centered Inertial (ECI) frame. The gravitational parameter is equal to the product of Newton's gravitational constant, G, and the mass of the Earth [30], given by

$$\mu = 3.98 * 10^5 \frac{km^3}{s^2}$$

Using the orbital elements to determine the positional and velocity components of the

12

system's orbit, the Keplerian equations of motion can be numerically solved to determine the motion of the system as a function of time. This depiction of the two-body equation of motion is simplified by assuming a spherical earth and neglects tidal forces [28].

2.3 Coordinate Systems

To accurately describe the kinematics of a tethered system, reference frames must be established to describe different coordinate systems. In this section, the applicable fixed and rotating reference frames are defined.

2.3.1 Earth Centered Inertial - ECI

The ECI frame is a *geocentric* Cartesian coordinate system with its origin at the center of the Earth with the unit vector $\hat{\mathbf{X}}$ towards the Vernal Equinox, the unit vector $\hat{\mathbf{Z}}$ normal to the fundamental plane of the equator, and the unit vector $\hat{\mathbf{Y}}$ completing the set, as seen in Figures 2.1 and 2.2. This reference frame remains fixed while the Earth rotates.

2.3.2 Perifocal

The perifocal coordinate system is a fixed reference frame centered at the focus of the orbit, in this case Earth, with the orbital plane as the fundamental plane. This system is considered the "natural frame" for an orbit [30]. The $\hat{\mathbf{x}}$ vector is in the plane in the direction of the periapsis, *i.e.,* along the eccentricity vector, and the $\hat{\mathbf{y}}$ vector is rotated $90°$ in the plane in the direction of orbital motion. The $\hat{\mathbf{z}}$ vector is normal to the orbital plane in the direction of the orbital angular momentum vector $\mathbf{h}$. These unit vectors are also often described with the notation $\mathbf{p}$, $\mathbf{q}$, and $\mathbf{w}$, for $\mathbf{x}$, $\mathbf{y}$, and $\mathbf{z}$, respectively [31].

Coordinate Transformation

Inertial differential equations are typically expressed in the perifocal frame but to understand the inertial position represented here, a rotation matrix is required to transfer the coordinates into the ECI frame. The transformation from the perifocal frame to the ECI frame can be accomplished with a 3-1-3 rotation sequence as follows:

1. Rotate the frame by ω about the angular momentum vector $\mathbf{h}$
2. Rotate by the frame by i about the vector in the direction of the ascending node $\mathbf{I}$

3. Rotate by the frame by Ω about the ECI's $\mathbf{z}$ unit vector

The composite rotation from the perifocal to the ECI frame is

$$\mathbf{r}_{ECI} = R_3(\Omega)R_1(i)R_3(\omega) \tag{2.2}$$

which gives the Direction Cosine Matrix (DCM) as described in [28] shown below:

$$\mathbf{C} = \begin{bmatrix} \cos\Omega\cos\omega - \sin\Omega\sin\omega\cos i & -\cos\Omega\sin\omega - \sin\Omega\cos\omega\cos i & \sin\Omega\sin i \\ \sin\Omega\sin\omega + \cos\Omega\sin\omega\cos i & -\sin\Omega\sin\omega + \cos\Omega\cos\omega\cos i & -\cos\Omega\sin i \\ \sin\omega\sin i & \cos\omega\sin i & \cos i \end{bmatrix} \tag{2.3}$$

2.3.3 Local Vertical Local Horizontal - LVLH

The Local Vertical Local Horizontal (LVLH) coordinate system is a *rotating* frame centered at the spacecraft. The fundamental plane is the orbital plane of the satellite, with the $\hat{\mathbf{z}}$ normal to the plane, pointing in the direction of the orbital momentum vector $\mathbf{h}$. The $\hat{\mathbf{x}}$ vector is in the plane, pointing radially outward from the spacecraft, as seen in Figure 2.2. The $\hat{\mathbf{y}}$ completes the set and points in along-track direction of instantaneous velocity. This frame is also known as Hill's frame [28]. In terms of formation flight, a deputy spacecraft is often described in terms of the chief's LVLH coordinates. This can be seen in Figure 2.2 where the $\mathbf{R}$ vector points to the chief satellite, and sets the origin by which the deputy position $\mathbf{r}$ is established. The LVLH unit vectors are derived from the position and velocity vectors in the ECI frame as follows [32]:

$$\hat{\mathbf{x}} = \frac{\mathbf{r_0}}{|r_0|} \tag{2.4}$$

$$\hat{\mathbf{z}} = \frac{\mathbf{h}}{|h|}, \quad \text{where} \quad \mathbf{h} = \mathbf{r_0} \times \mathbf{v_0} \tag{2.5}$$

$$\hat{\mathbf{y}} = \hat{\mathbf{z}} \times \hat{\mathbf{x}} \tag{2.6}$$

The DCM to convert from ECI vectors to LVLH vectors is

$$\begin{bmatrix} ON \end{bmatrix} = \begin{bmatrix} \hat{\mathbf{x}}^{\mathbf{T}} \\ \hat{\mathbf{y}}^{\mathbf{T}} \\ \hat{\mathbf{z}}^{\mathbf{T}} \end{bmatrix} \tag{2.7}$$
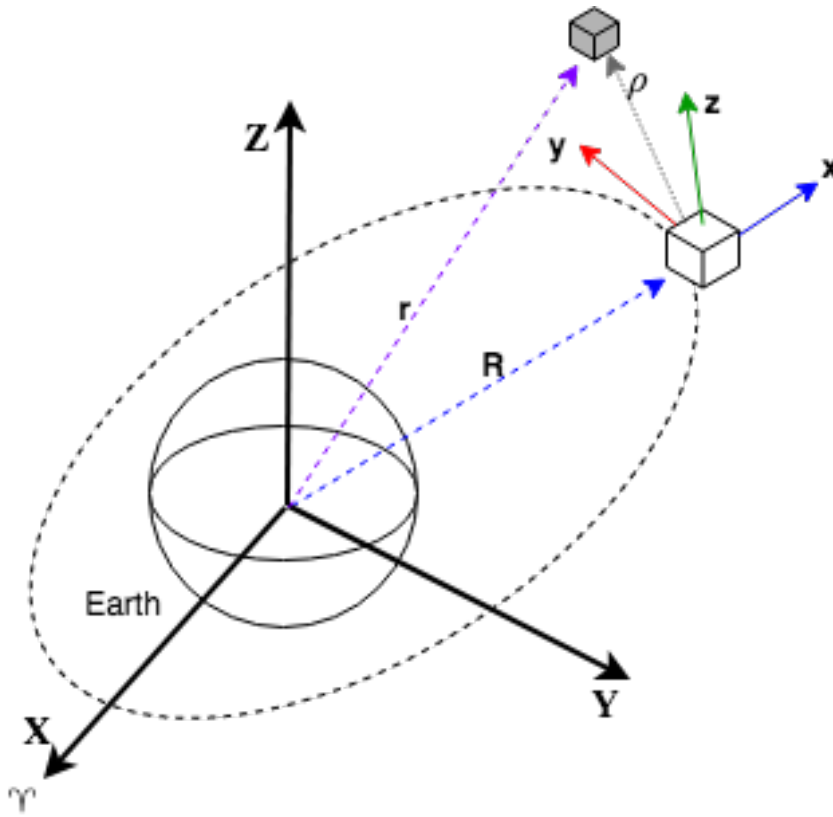
14

Figure 2.2. Chief and Deputy Spacecraft Local Vertical-Local Horizontal with ECI Frame

2.4 Satellite Relative Motion

Relative motion is the depiction of the movement of a satellite with respect to another satellite. For convention, the debris removal satellite that will be used for reference will be referred to throughout as the *chief*, and the object, or uncontrolled debris, whose motion is described in terms of the chief, will be referred to as the *deputy*. The position of the chief satellite is denoted by the vector **R** and the position of the deputy is denoted by the vector **r**. The vector describing the displacement between the two satellites is denoted by the vector ρ shown in Figure 2.2. The chief position vector in the LVLH frame is described by the following equation:

$$\mathbf{R} = R\hat{i} \tag{2.8}$$

15

and the deputy relative position vector can be described as

$$\mathbf{r} = \mathbf{R} + \boldsymbol{\rho} \qquad (2.9)$$

where

$$\boldsymbol{\rho} = x\hat{i} + y\hat{j} + z\hat{k},$$

and therefore

$$\mathbf{r} = (R + x)\hat{i} + y\hat{j} + z\hat{k} \qquad (2.10)$$

Using these relative positions, the nonlinear and linearized equations of relative motion are derived in Chapter 4. Additionally, Appendix A contains an exploration of different methods of propagating relative motion using the Clohessy-Wiltshire and Tschauner-Hempel equations [28]. The Clohessy-Wiltshire method provides a simplified technique to solve the relative motion propagation of a circular orbit, but the Tschauner-Hempel equations can provide a more general simplified solution for any orbit using what is known as the Yamanaka-Ankersen method [33].

CHAPTER 3:
Orbital Debris Lifetime Analysis

In order to assess how ADR methods can impact a debris object, a baseline lifetime analysis was conducted on the candidate debris. The lifetime is determined as a function of orbital characteristics, spacecraft drag area, and atmospheric drag. The National Centre for Space Studies (CNES) developed software Semi-analytic Tool for End of Life Analysis (STELA) was used to conduct the lifetime analysis [34].

3.1 Debris Characteristics

The debris modeled throughout this study has the characteristics presented in Table 3.1 based loosely on those of Hubble Space Telescope [35]. For the purpose of maintaining a simple model, the debris will be modeled as a sphere, as will any debris removal vehicle. As the orbit represented here is circular, the terms altitude and semi-major axis are used interchangeably.

Table 3.1. Debris Characteristics

Mass	10,000 kg
Sphere radius	5 m
Mean drag area	78.6 m^2
Epoch	August 15, 2018 21:40:27 UTC
Inclination	28.5°
Semi-major axis	6878 km
Eccentricity	0
Right Ascension of the Ascending Node (RAAN)	80°
Argument of perigee	65°
Mean Anomaly	24°

Additionally, it is assumed that despite the relatively short predicted lifetime of the debris, uncontrolled reentry is not an option due to the associated risks to humans on the ground. A reentry survivability assessment of Hubble performed in 2005 predicts a reentry risk of 1:250, which well exceeds the acceptable risk of 1:10,000 [36], [37].

3.2 Debris Lifetime Analysis

To determine the effect of increasing drag area on the debris, STELA was used to iteratively increase the drag area and determine the impact on orbital lifetime. Without drag area augmentation, the debris will reenter the atmosphere approximately 4.45 years from the start date epoch. While this is in compliance with DoDI 3100.12 section 6.4.1, the accepted practice of decaying within 25 years upon completion of missions, it is assumed that an uncontrolled entry is not an acceptable option due to reentry casualty risk, and therefore, additional mitigation measures must be taken to facilitate reentry at a specific point. When an additional 100 m^2 are added to the debris, the debris decays in 3.44 years, as shown in Figure 3.1. This suggests that this debris object is relatively insensitive to drag area augmentation alone. The atmospheric model used to model atmospheric drag was NRLMSISE-00 and the solar activity was variable beginning from the epoch listed in Table 3.1.
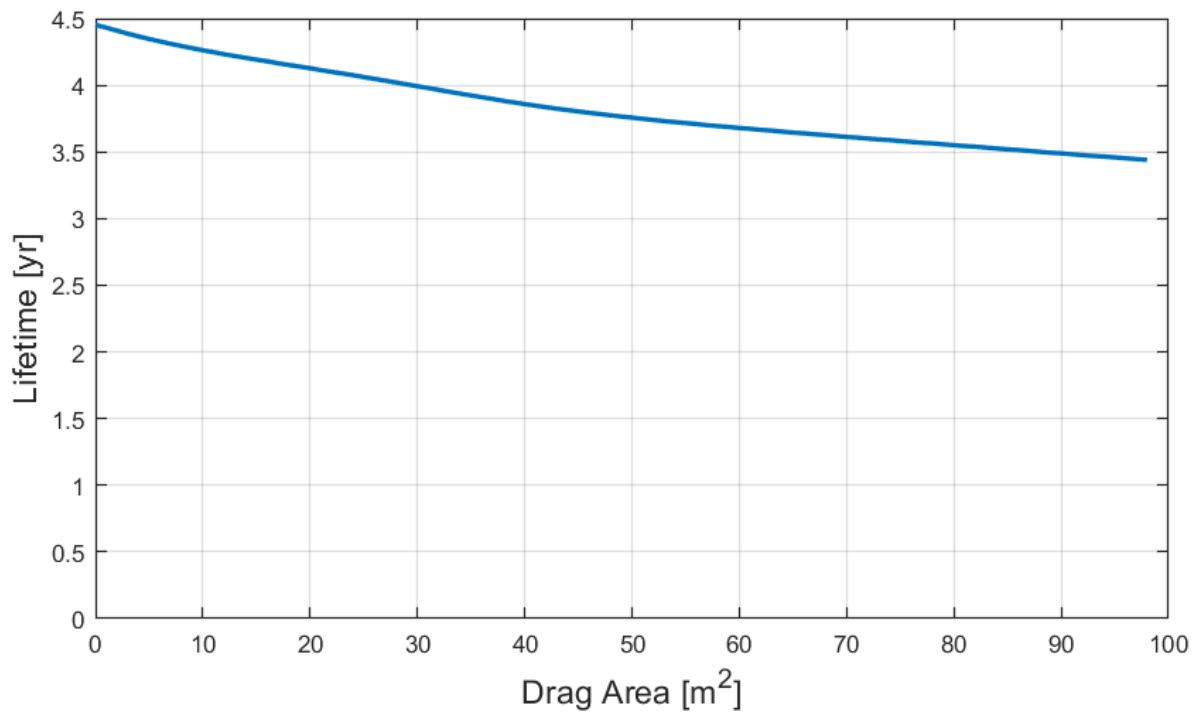
Figure 3.1. Effect of Increasing Drag Area on Orbital Lifetime

The data presented in Figure 3.2 shows the same analysis as the previous, but the starting altitude was set 50 km lower than the baseline to represent a 50 km drag tether, represented as the red line. This data shows that with an additional 100 m^2, the orbital lifetime can be reduced to 2.44 years. These lines display a near parallel trend, and the average difference in lifetime as area increases is about one year. The red axis below the axis displaying total drag area increase shows the total spherical radius of the object given by the increased drag area.
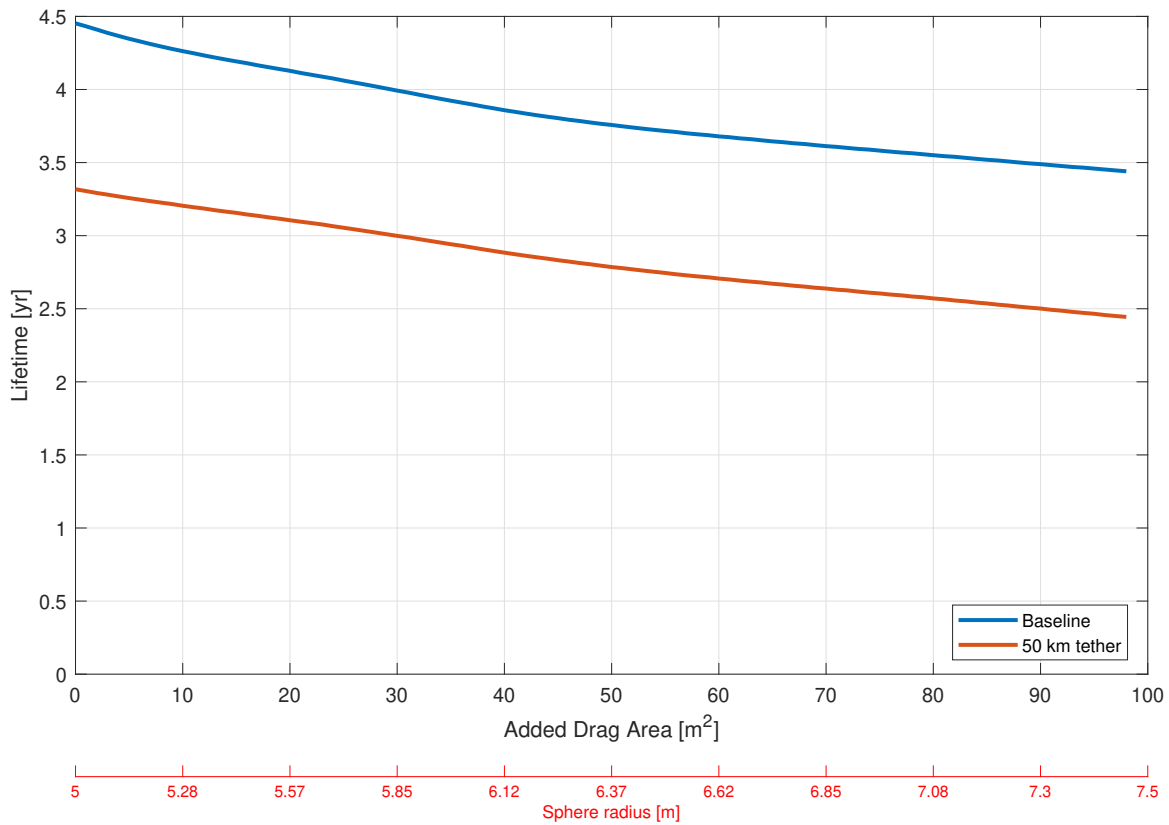
Figure 3.2. Effect of Increasing Drag Area on Orbital Lifetime - 50 km Tether Comparison

To observe the effect of tether length over lifetime with the addition of a drag augmentation system, i.e., a drag sail, a spherical object with a fixed radius of 10 m was assessed. The mass remained constant at 10,000 kg as drag sails are relatively light and its mass addition can be negligible. To simulate increasing tether length, the starting altitude of the object's orbit was iteratively decreased, and the lifetime for each discrete iteration was determined. The data presented in Figure 3.3 suggests that with a 70 km tether, a spherical object with a 10 m radius could reenter Earth's atmosphere within a year.
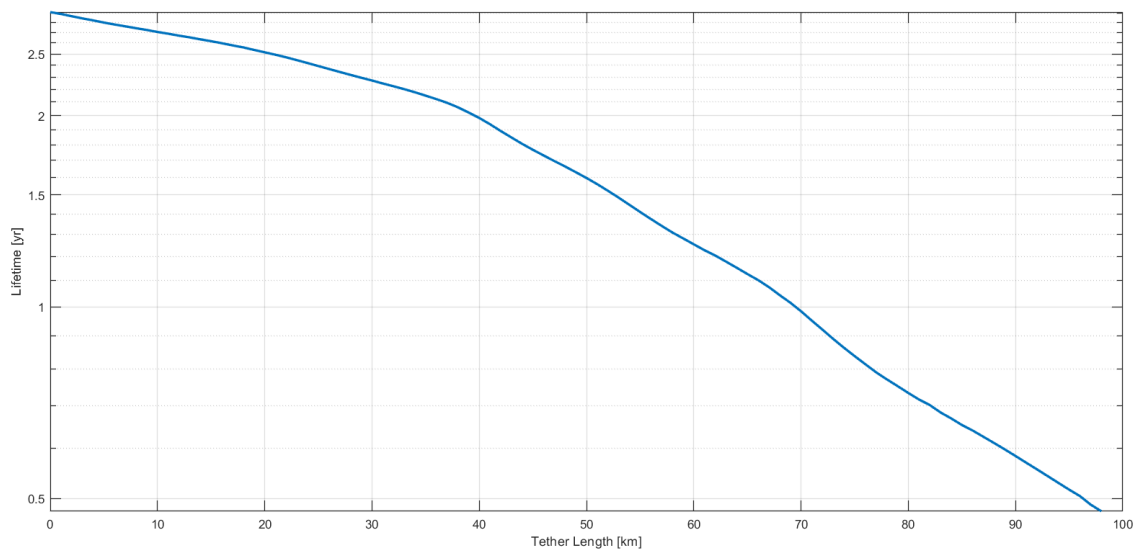
Figure 3.3. Effect of Increasing Tether Length on Orbital Lifetime - 10 m Sphere Radius

THIS PAGE INTENTIONALLY LEFT BLANK

CHAPTER 4:
Derivation of Tethered Relative Motion Equations

To understand and manipulate the orbit of a tethered satellite system, a useful model of a tethered system must be developed. In this chapter, first the non-linear and linearized equations of relative motion for an un-tethered system of two satellites are derived. Subsequently the tether dynamics are considered to develop the relative equations of motion of a tethered satellite system.

4.1   Relative Motion

The acceleration of the chief satellite is determined by the twice differentiation of Equation (2.8)

$$\dot{\mathbf{R}} = \dot{R}\mathbf{i} + R\dot{v}\mathbf{j} \tag{4.1}$$

$$\ddot{\mathbf{R}} = (\ddot{R} - R\dot{v}^2)\mathbf{i} + (2\dot{R}\dot{v} + R\ddot{v})\mathbf{j} \tag{4.2}$$

Differentiation for deputy vehicle position in equation (2.10)

$$\dot{\mathbf{r}} = (\dot{R} + \dot{x} - \dot{v}y)\mathbf{i} + (\dot{v}R + \dot{v}x + \dot{y})\mathbf{j} + \dot{z}\mathbf{k} \tag{4.3}$$

$$\ddot{\mathbf{r}} = (\ddot{R} - \dot{v}^2 R + \ddot{x} - \dot{v}^2 x - \ddot{v}y - 2\dot{v}\dot{y})\mathbf{i} + (\ddot{v}R + 2\dot{v}\dot{R} + \ddot{v}x + \ddot{y} + 2\dot{v}\dot{x} - \dot{v}^2 y)\mathbf{j} + \ddot{z}\mathbf{k} \tag{4.4}$$

To put the equations of motion in terms of the gravitational force, we employ the simplified two-body problem described in Equation 2.1. For the chief satellite, this equates to

$$\ddot{\mathbf{R}} = \frac{-\mu}{R^3}\mathbf{R} = \frac{-\mu}{R^2}\mathbf{i} \tag{4.5}$$

and for the deputy satellite

$$\ddot{\mathbf{r}} = \frac{-\mu}{r^3}[(R + x)\mathbf{i} + y\mathbf{j} + z\mathbf{k}] \tag{4.6}$$

The deputy equations of motion can be broken into its x, y, and z components as follows:

$$\frac{-\mu}{R^2} + \ddot{x} - \ddot{\nu}y - 2\dot{\nu}\dot{y} - \dot{\nu}^2 x = \frac{-\mu}{r^3}(R + x) \tag{4.7}$$

$$\ddot{y} + 2\dot{\nu}\dot{x} + \ddot{\nu}x - \dot{\nu}^2 y = \frac{-\mu}{r^3}y \tag{4.8}$$

$$\ddot{z} = \frac{-\mu}{r^3}z \tag{4.9}$$

4.1.1 Linearized Equations of Motion

Equations (4.7) to (4.9) are the nonlinear forms of the equations of motion. To develop a simpler model to analyze and understand dynamic motion of the system, the equations of motion are linearized to approximate the $\frac{1}{r^3}$ term. To do this, we consider the magnitude of the deputy position vector, as described in Equation (2.10).

$$|\mathbf{r}| = \sqrt{[(R + x)^2 + y^2 + z^2]} \tag{4.10}$$

Expanded, this can be expressed as

$$|\mathbf{r}| = (R^2 + 2Rx + x^2 + y^2 + z^2)^{\frac{1}{2}} \tag{4.11}$$

and further simplified as

$$|\mathbf{r}| = R(1 + \frac{2x}{r} + \frac{x^2 + y^2 + z^2}{R^2})^{\frac{1}{2}} \tag{4.12}$$

The third term can be eliminated due to the fact that $|\rho| \ll |\mathbf{R}|$ because the distance between the chief and deputy is much smaller than the distance from the chief to the center of the Earth. So the r^3 term can be represented as

$$r^3 = R^3(1 + \frac{2x}{R})^{\frac{3}{2}} \tag{4.13}$$

which finally results in the binomial form that can be used for the approximation via the Taylor Series expansion

$$\frac{1}{r^3} = \frac{1}{R^3}(1 + \frac{2x}{R})^{\frac{-3}{2}} \tag{4.14}$$

24

The Taylor series expansion for the binomial $(1 + x)^n$ is as follows:

$$(1 + x)^n = 1 + nx + \frac{n(n-1)}{2!}x^2 + \dots \tag{4.15}$$

This results in the approximation

$$\frac{1}{r^3} \approx \frac{1}{R^3}[1 + \frac{-3}{2}(\frac{2x}{R})] \tag{4.16}$$

and simplified:

$$\frac{1}{r^3} \approx \frac{1}{R^3}[1 + \frac{3x}{R}] \tag{4.17}$$

The substitution of this approximation into the nonlinear equations of motion results in the following linearized equations of motion.

$$\ddot{x} - 2\dot{v}y - \ddot{v}y - \dot{v}^2x - 2\frac{\mu x}{R^3} = 0 \tag{4.18}$$

$$\ddot{y} + 2\dot{v}\dot{x} + \ddot{v}x - \dot{v}^2y + \frac{\mu}{R^3}y = 0 \tag{4.19}$$

$$\ddot{z} + \frac{\mu}{R^3}z = 0 \tag{4.20}$$

When the chief satellite is in a circular orbit, these equations can be further simplified, knowing that true anomaly and Mean anomaly are identical [30], so $v = nt$, then $\dot{v} = n$, and therefore $\dot{f}^2 = n^2 = \frac{\mu}{R^3}$ and $\ddot{v} = 0$ and result in the following equations:

$$\ddot{x} - 2n\dot{y} - 3\frac{\mu}{R^3}x = 0 \tag{4.21}$$

$$\ddot{y} - 2n\dot{x} = 0 \tag{4.22}$$

$$\ddot{z} + n^2z = 0 \tag{4.23}$$

which are known as the Clohessy-Wiltshire equations [28]. These equations are often used for propagations of orbits of multiple bodies in close proximity, applied for use in rendezvous missions or formation flying [30]. They are, however, limited in that they only provide solutions for a chief spacecraft in a circular orbit. An in-depth comparison of relative motion propagation methods for formation flight is included in Appendix A, and

includes arbitrarily elliptic orbits.

4.2   Tethered Relative Motion

As can be seen in Figure 4.1, the tethered satellite motion must include the restoring force component from the tether tension.
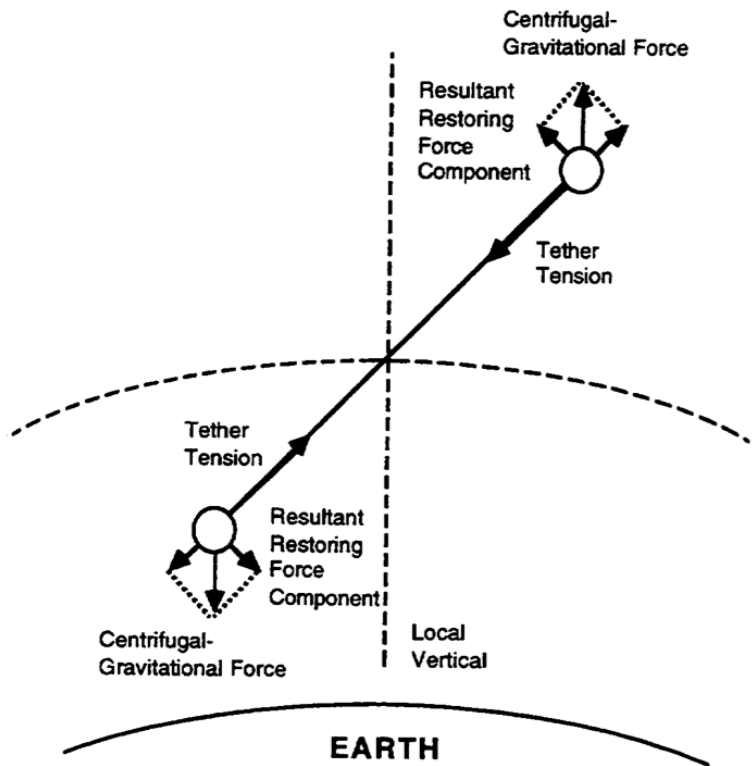

Figure 4.1. Restoring Forces on TSS. Source: [25].

Therefore, a similar derivation method as in Section 4.1 was completed, but with the addition of the tether tension force. Here it is assumed that the tether is massless, rigid, and each spacecraft in the tethered formation can be represented as a point mass. Again, by applying the simplified two-body problem, the equation of motion for the deputy spacecraft is

$$m\ddot{\vec{r}} = -m\frac{\mu\vec{r}}{r^3} + (\vec{F}_t) \tag{4.24}$$

26

where $(\vec{F}_t)$ is the tether tension between the deputy and chief elements. The chief equation of motion is

$$m_c \ddot{\vec{R}} = -m_c \frac{\mu \vec{R}_c}{R_c^3} + (\vec{F}_t)_c \tag{4.25}$$

4.2.1 Tether Tension Force

The tether can be modeled as an elastic linear spring and the tether tension force can be determined by applying Hooke's law to the tether parameters. The tether tension force can be described as

$$\mathbf{F_t} = \frac{EA}{l_0} [(|\mathbf{R} - \mathbf{r}) - l_0] \tag{4.26}$$

where E is the modulus of elasticity of the tether, A is the cross-sectional area of the tether, and, l_0 is the unstretched tether length [38].

4.2.2 Equations of Motion of a Spinning Spacecraft Tethered System

The relationship between the spin and LVLH axes can be described as a primary rotation around the z axis.

$$\begin{bmatrix} x \\ y \\ z \end{bmatrix} = \begin{bmatrix} \cos\theta & -\sin\theta & 0 \\ \sin\theta & \cos\theta & 0 \\ 0 & 0 & 1 \end{bmatrix} \begin{bmatrix} x_s \\ y_s \\ z_s \end{bmatrix} \tag{4.27}$$

This relationship can be broken into its radial, along-track, and cross-track components and differentiated twice to substitute into the system of equations in Equations (4.18) to (4.20). The radial relationship is as follows:

$$x = \cos\theta x_s - \sin\theta y_s \tag{4.28}$$

$$\dot{x} = -\dot{\theta} \sin\theta x_s + \cos\theta \dot{x}_s - \dot{\theta} \cos\theta y_s - \sin\theta \dot{y}_s \tag{4.29}$$

$$\ddot{x} = (-\ddot{\theta} \sin\theta - \dot{\theta}^2 \cos\theta) x_s - 2\dot{\theta} \sin\theta \dot{x}_s + \cos\theta \ddot{x}_s + (-\ddot{\theta} \cos\theta + \dot{\theta}^2 \sin\theta) y_s - 2\dot{\theta} \cos\theta \dot{y}_s - \sin\theta \ddot{y}_s \tag{4.30}$$

The along-track relationship between the spin and LVLH axes is:

$$y = \sin\theta x_s + \cos\theta y_s \tag{4.31}$$

$$\dot{y} = \dot{\theta}\cos\theta x_s + \sin\theta \dot{x}_s - \dot{\theta}\sin\theta y_s - \cos\theta \dot{y}_s \tag{4.32}$$

$$\ddot{y} = \cos\theta \ddot{y}_s + \sin\theta \ddot{x}_s + 2\dot{\theta}\dot{x}_s - 2\dot{\theta}\sin\theta \dot{y}_s + (\ddot{\theta}\cos\theta - \dot{\theta}^2\sin\theta)x_s + (-\ddot{\theta}\sin\theta + \dot{\theta}^2 sin\theta)y_s \tag{4.33}$$

And finally, the cross-track relationship and twice-differentiation

$$z = z_s \tag{4.34}$$

$$\dot{z} = \dot{z}_s \tag{4.35}$$

$$\ddot{z} = \ddot{z}_s \tag{4.36}$$

To determine the spinning tethered spacecraft relative motion equations, the spin relationship presented above was substituted into the linearized tethered equations of motion. As the cross-track equations directly correlate, only the radial and along-track substitution will be presented here. The radial component is

$$\cos\theta \ddot{x}_s - \sin\theta \ddot{y}_s - 2\dot{\theta}\sin\theta \dot{x}_s - 2\dot{\theta}\cos\theta \dot{y}_s - \ddot{\theta}\sin\theta x_s - \dot{\theta}^2\cos\theta x_s - \ddot{\theta}\cos\theta y_s + \dot{\theta}^2\sin\theta y_s$$
$$- 2\dot{v}\dot{\theta}\cos\theta x_s - 2\dot{v}\sin theta \dot{x}_s + 2\dot{v}\dot{\theta}\sin\theta y_s - 2\dot{v}\cos\theta \dot{y}_s - \ddot{v}\sin\theta x_s - \ddot{v}\cos\theta y_s - \dot{v}^2\cos\theta x_s$$
$$+ \dot{v}^2\sin\theta y_s - 2\frac{\dot{v}^2}{1 + e\cos v}\cos\theta x_s + 2\frac{\dot{v}^2}{1 + e\cos v}\sin\theta y_s = \frac{f_x}{m_j} \tag{4.37}$$

The along-track component is

$$\cos\theta \ddot{y}_s + \sin\theta \ddot{x}_s - 2\dot{\theta}\sin\theta \dot{y}_s + 2\dot{\theta}\cos\theta \dot{x}_s - \ddot{\theta}\cos\theta x_s - \dot{\theta}^2\sin\theta x_s - \ddot{\theta}\sin\theta y_s + \dot{\theta}^2\cos\theta y_s$$
$$- 2\dot{v}\dot{\theta}\sin\theta x_s + 2\dot{v}\cos theta \dot{x}_s - 2\dot{v}\dot{\theta}\cos\theta y_s - 2\dot{v}\sin\theta \dot{y}_s + \ddot{v}\cos\theta x_s - \ddot{v}\sin\theta y_s - \dot{v}^2\sin\theta x_s$$
$$- \dot{v}^2\cos\theta y_s + 2\frac{\dot{v}^2}{1 + e\cos v}\sin\theta x_s + 2\frac{\dot{v}^2}{1 + e\cos v}\cos\theta y_s = \frac{f_y}{m_j} \tag{4.38}$$

To simplify, the $\ddot{x}$ and $\ddot{y}$ terms must be isolated by taking advantage of the trigonometric identity $\sin^2\theta + \cos^2\theta = 1$. To isolate $\ddot{x}$, the radial component of the equation of motion

28

was multiplied by $\cos\theta$ and the along-track component was multiplied by $\sin\theta$, and these equations combined to result in the following.

$$\ddot{x}_s - 2(\dot{v} + \dot{\theta})\dot{y}_s + \left[\frac{\dot{v}^2}{1 + e\cos v}(1 - 3\cos^2\theta) - (\dot{v} + \dot{\theta})^2\right]x_s - \ddot{v}y_s$$
$$+ \left(3\frac{\dot{v}^2}{1 + e\cos v}\sin\theta\cos\theta\right)y_s = \cos\theta\frac{f_x}{m_j} + \sin\theta\frac{f_y}{m_j} \quad (4.39)$$

Similarly, the along-track component was found by isolating the $\ddot{y}$ term by multiplying the radial component by $\sin\theta$ and the along-track component by $\cos\theta$ and combining the equations to result in the following

$$\ddot{y}_s + \ddot{v}x_s + 2(\dot{v} + \dot{\theta})\dot{x}_s + 3\frac{\dot{v}^2}{1 + e\cos v}\cos\theta\sin\theta x_s + (\frac{\dot{v}^2}{1 + e\cos v}(3\cos^2\theta - 2)$$
$$- (\dot{v} + \dot{\theta})^2) = \cos\theta\frac{f_y}{m_j} - \sin\theta\frac{f_x}{m_j} \quad (4.40)$$

The cross track component of the spinning tethered equations of motion is

$$\ddot{z}_s + \frac{\dot{v}^2}{1 + e\cos v}z_s = \frac{f_z}{m_j} \quad (4.41)$$

This derivation of tethered relative motion offers useful insight into how the Tethered Satellite System (TSS) orbit propagates and each end-body interacts with the other. However, due to the added complexity of tethered relative motion, and for consistency with the majority of current study, the system utilized in this thesis was ultimately modeled as a rigid body dumbbell system with the orbital characteristics described from the system's center of mass. The dumbbell dynamics are described in the following chapter.

THIS PAGE INTENTIONALLY LEFT BLANK

CHAPTER 5:
Momentum Exchange Tethered Debris Removal

Typical studies of tethered momentum exchange systems involve a propellantless method of orbital transfer. For a debris removal system, instead of transferring the object to a higher orbit, the object would be transferred into either a decay orbit or an Earth-impacting trajectory for targeted re-entry. As with the "TAMU sling sat sweeper," certain momentum exchange orbital transfer methods use the capture velocity of the transferring payload to begin the momentum exchange process [16], [25]. Additional applications include formation stationkeeping via satellites exchanging momentum in the form of radiation or mass. An attractive force from tethers between satellites creates an almost rigid formation, which allows for several geometric configurations, applicable across a multitude of missions [39]. The method studied in this thesis explores a tether retrieval maneuver to increase the angular velocity of the system, exploiting the principle of conservation of angular momentum.

The angular momentum of a rotating rigid body system is defined as

$$\mathbf{H} = \mathbf{J}\omega_{\mathbf{BN}} \tag{5.1}$$

where $\mathbf{H}$ is the angular momentum of the system, $\mathbf{J}$ is the moment of inertia of the rigid body, and $\omega_{\mathbf{BN}}$ is the angular velocity of the body frame relative to the inertial frame of the system.

As the tether is retrieved, the moment of inertia, J, of the system decreases, and the angular velocity of the system increases. At the desired ω , the tether is separated, imparting ΔV to both satellites. While attached, the momentum of the system is conserved, but the act of momentum exchange occurs when the end mass is released.

$$H_{sys} = H_1 + H_2 \tag{5.2}$$

The librational motion of the TSS, caused by gravity, can dictate the speed of the debris object's release and can be controlled by changing the tether length [19]. A tethered debris

removal system would use the retrieval of the tether to increase the angular velocity of the system and then release the debris once the appropriate ΔV could be attained [40].

5.1 Debris Reentry Considerations

In order to determine the ΔV required to be generated from the momentum exchange system, the following equation was used to determine the ΔV required to drop a satellite from its initial circular altitude h_i to a reentry perigee altitude h_e of 120 km. [41] The final perigee altitude is typically the standard reentry threshold for space vehicles. In order to deorbit debris, the debris orbit perigee must intersect the Earth's atmosphere upon release. [42] The initial orbital elements used for this analysis are the same as those presented in Table 3.1.

$$\Delta V_{deorbit} \approx V \left[1 - \sqrt{\frac{2(R_E + h_e)}{2R_E + h_e + h_i}} \right] \tag{5.3}$$

where V is the initial debris velocity. As the debris for the model is in a circular orbit, the orbital velocity is constant and can be found with the following:

$$v_{circular} = \sqrt{\frac{\mu}{r}} = 7.6127 \ km/s \tag{5.4}$$

From this calculation, the required $\Delta V_{deorbit}$ is 108.9 m/s. This is equal to the result from a Hohmann transfer calculation. If the desired trajectory is impact with earth, the final perigee altitude must be less than or equal to the radius of the earth. This would require a ΔV of 145 m/s. Simply by extending the tether and decreasing the orbital radius of the debris, it will experience a change in velocity when separated. The effects of tether length on ΔV will be discussed in Section 5.4.

5.2 System Model

Due to the complexity of the equations of relative motion shown in Chapter 4, the system was ultimately modeled as a rigid-body system with a rigid, massless, extensible tether in a dumbbell configuration connecting the two spherical masses, the debris object and the debris removal vehicle, at each object's center of mass, as shown in Figures 5.1 and 5.2. It is assumed that the tether can be extended or retracted with some form of reel mechanism
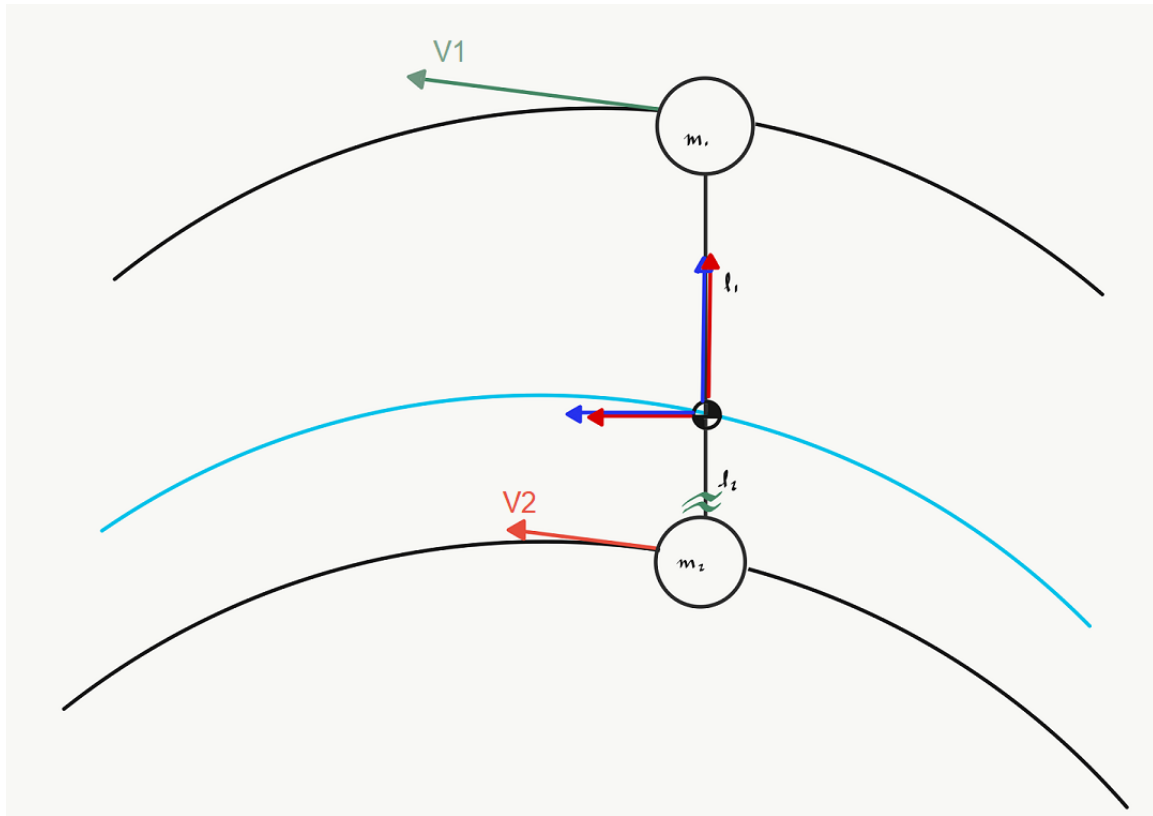
at the debris removal vehicle.

Figure 5.1. Angular Momentum of Tethered Dumbbell System

The orbital motion of the system will be described from the system mass center, which continues to orbit at the initial circular altitude of 6878 km. For simplicity, center of mass and center of gravity will be considered to be the same position. Using the following center of mass equation, the distance from the debris object to the center of mass is determined:

$$L_{debris\ to\ COM} = \frac{m1 * l_0}{(m1 + m2)} \tag{5.5}$$

where $m1$ is the mass of the debris Service Vehicle (SV), $m2$ is the mass of the debris, and L_0 is the total length of the tether.

The body fixed reference frame of the system is aligned with the principal axes of inertia. Given the tether is assumed to be massless, the tether mass does not affect the inertia of the system. Aligning the x axis of the body frame along the rigid tether as seen in Figure

5.2, and calculating the moments of inertia for each spacecraft as a solid sphere, the inertia tensor of the system in the body-fixed reference frame can be described as

$$\mathbf{J} = \begin{bmatrix} \frac{2}{5}m_1r_1^2 + \frac{2}{5}m_2r_2^2 & 0 & 0 \\ 0 & m_2l_2^2 + m_1l_1^2 & 0 \\ 0 & 0 & m_2l_2^2 + m_1l_1^2 \end{bmatrix} \tag{5.6}$$

where m_1 is the mass of the SV, m_2 is the mass of the debris, r_1 is the radius of the SV, l_1 is the distance from the system center of mass to the SV center of mass, r_2 is the radius of the debris, l_2 is the distance from the system center of mass to the debris center of mass. By aligning the tether direction along the x axis, when the pitch angle (or libration angle, β) is 0, the body frame is aligned with the orbital LVLH frame.
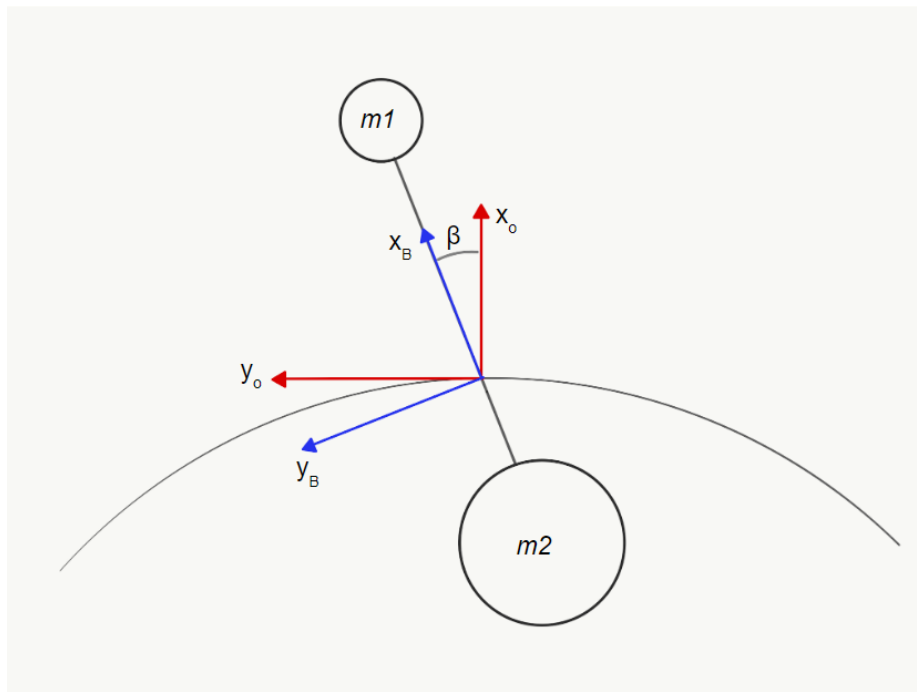

Figure 5.2. Body Frame of Dumbbell Tethered System

This body fixed frame was chosen in order to utilize a diagonal inertia tensor as seen in Equation (5.6).

5.3　Tethered System Rigid Body Dynamics

If the dynamics of the two end bodies were considered individually, and both were modeled in Keplerian circular orbits, it could be seen that the body in a higher altitude moves at a slower speed than the lower mass. The addition of the tether causes the upper mass to experience a greater centrifugal force than gravitational and the lower to accordingly experience larger gravitational acceleration than centrifugal force creating the balanced tether tension and the restoring librational motion [25]. A visualization of these forces is shown in Figure 4.1. In this thesis, only in-plane librational motion will be considered.

The natural frequency of the in-plane libration can be defined as $\sqrt{3} * n$ where n is the mean orbital motion [25] [40]. This is due to the gravity gradient restoring torques experienced naturally by the system.

5.3.1　Rotational Kinematics

The angular velocity of the LVLH orbital frame shown in Figure 2.2 relative to the inertial ECI frame can be described as

$$\omega_{\mathbf{on}} = \dot{v}\hat{\mathbf{z}} \tag{5.7}$$

where $\dot{v}$ is the rate of change of true anomaly. For circular orbits, this is equal to n, the mean motion of the orbit and can be defined as:

$$n = \sqrt{\frac{\mu}{a^3}} \tag{5.8}$$

and $\hat{\mathbf{z}}$ is the unit vector parallel to the orbit momentum vector in the LVLH frame, as described in Section 2.3.3 [32].

As the Euler rotational equations of motion apply to the body frame of the system, the initial angular velocity of the spacecraft relative to the inertial frame must be determined by the following:

$$\omega_{\mathbf{BN}} = \omega_{\mathbf{BO}} + \omega_{\mathbf{ON}}$$

Following this definition, ω will refer to the body rotational velocity ω_{BN}. To observe the rotational dynamics of the rigid body tether system, the Euler Rotational Equations of motion were solved for the spin rate of the body, $\dot{\omega}$ using a Runge-Kutta method. Euler's

rotational equations of motion are typically written as

$$\mathbf{J}\dot{\omega} + \omega \times \mathbf{J}\omega = \mathbf{T} = \dot{\mathbf{H}} \tag{5.9}$$

where M are the external moments (or torques) acting about the mass center. However, the short form of Euler's equations do not capture the entirety of this scenario, and the rate of change of the inertia tensor of the system must be accounted for. Therefore, Euler's rotational equations of motion for a TSS with changing tether length can be expressed as

$$J\dot{\omega} + \dot{J}\omega + \omega \times J\omega = T = \dot{H} \tag{5.10}$$

The differential equation of the system dynamics (5.11) was numerically integrated to find the angular velocity of the system. The system Simulink model is provided in

$$\dot{\omega} = -J^{-1}\left(T - \dot{J}\omega - \omega \times J\omega + T\right) \tag{5.11}$$

5.3.2 Gravity Gradient

As the gravitational force does not vary linearly, the system experiences different gravitational forces along its body. This condition is often used to stabilize nadir-pointing satellites, e.g., the moon [32]. When the system is not aligned with local vertical, i.e., has an initial pitch angle, β, the gravity gradient torque provides a restoring force to return the TSS to the stable vertical condition [25]. When the system is in a stable in-plane spin, the restoring gravity gradient torque behaves in an oscillatory manner, as seen in Figure 5.4.

The gravity gradient torque can be determined in terms of its body-frame components [43]

$$T_{gg} = \frac{3\mu}{R^3} \begin{Bmatrix} \left(J_z - J_y\right) c_2 c_3 \\ \left(J_x - J_z\right) c_1 c_3 \\ \left(J_y - J_x\right) c_1 c_2 \end{Bmatrix} \tag{5.12}$$

where c_1, c_2, and c_2 are the direction cosines of the local vertical relative to the body triad [44].

36

The system attitude can be described in terms of its quaternion, or Euler parameters. These parameters describe the rotation of the body relative to the ECI frame in terms of the Euler axis e and a rotation angle, β [43]. For this model, as the rotation occurs solely in the orbital plane, and about the body $\hat{z}$ axis, the quaternion can be described as in Equation (5.13).

$$q_{bn} = \begin{bmatrix} 0 \\ 0 \\ \sin\frac{\beta}{2} \\ \cos\frac{\beta}{2} \end{bmatrix} \tag{5.13}$$

5.4 Momentum Exchange Simulation Results

Assuming the debris is released when the system is aligned with the local vertical, the velocity of each end body at tether separation is determined in [40] as

$$V1 = R_0\omega_n + \left(\frac{m_2}{M}\right)\frac{(\omega_n + \dot{\beta})}{(1 - \Delta L/L)}L \tag{5.14}$$

$$V2 = R_0\omega_n - \left(\frac{m_1}{M}\right)\frac{(\omega_n + \dot{\beta})}{(1 - \Delta L/L)}L \tag{5.15}$$

To establish a baseline, the model was evaluated with the tether fully extended and the system librating at the natural libration rate of $\sqrt{3}n$. The debris experiences a ΔV of 13.7449 m/s, which, as established in Section 5.1, is insufficient for a terminal orbit. Therefore, the angular velocity of the TSS must be increased to attain the desired ΔV.

For observing in-plane motion, the pitch rate is the main body parameter of interest, as roll and yaw components of the attitude will affect the out-of-plane angular velocity components ω_y and ω_x, respectively. The pitch rate, $\dot{\beta}$, therefore corresponds to the z-component of the angular velocity of the body, ω_z, and the terms $\dot{\beta}$, ω_z, and ω may be used interchangeably. To ensure system rotation, the initial spin was set to $2\omega_n$ [40]. The initial conditions for the simulation are provided in Table 5.1.

Table 5.1. Initial Conditions for Momentum Exchange Maneuver

Parameter		Value
Initial Tether Length	L_0	50 km
Initial Pitch Angle	β_0	0.01 rad
Orbit Angular Velocity	ω_n	0.0011 rad/s
Initial Spin Rate	ω	$2*\omega_n$
System Mass	m_0	225000 kg
Tether Retrieval Rate	δL	1.4 m/s
Simulation Time	5 Orbits	28,348 s

A summary of the simulation results is provided in Figures 5.3 to 5.8.

The rate of change of the system inertia was determined numerically. Figure 5.3 shows the effect of decreasing tether length on total system inertia. As the inertia tensor is aligned with the body, only the y and z components of the system inertia are effected.
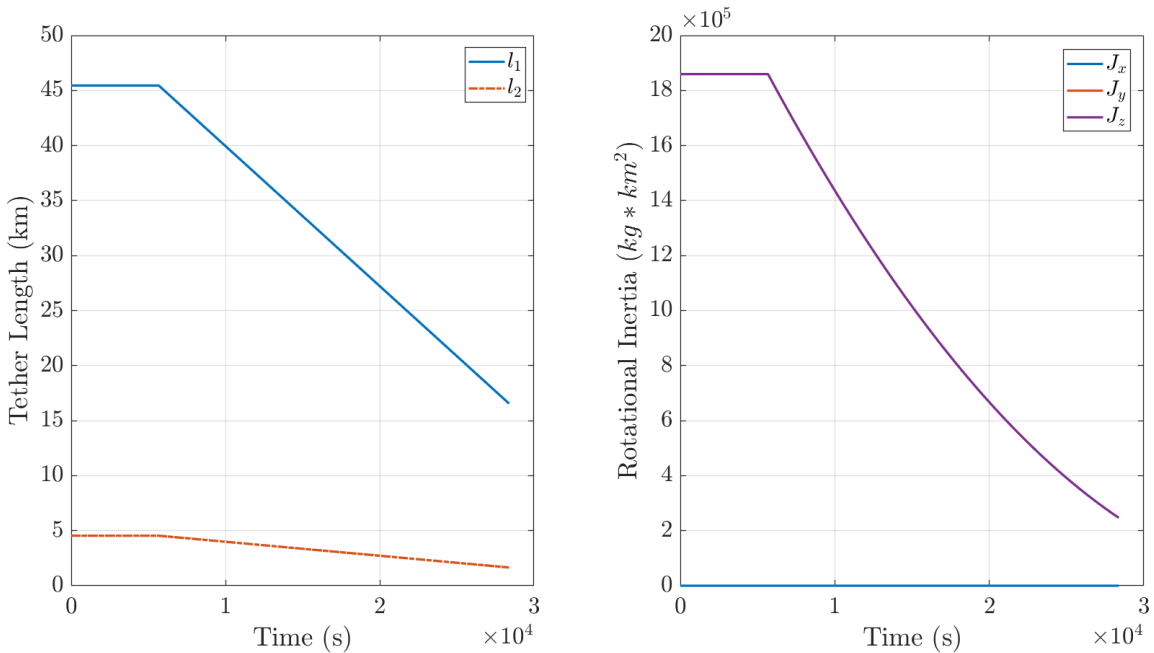
Figure 5.3. Total System Inertia and Component Tether Length

Over the simulation, the tether length decreased from 50km to 18.21 km and the total system

inertia decreased by 87 percent.

Figure 5.4 shows the gravity gradient torque on the TSS throughout the spin-up maneuver. The direction of the torque oscillates as the tether retrieval begins and the TSS angular velocity increases. As the tether length shortens, the torque decreases in magnitude, as there is less of a gravity gradient between each end body.
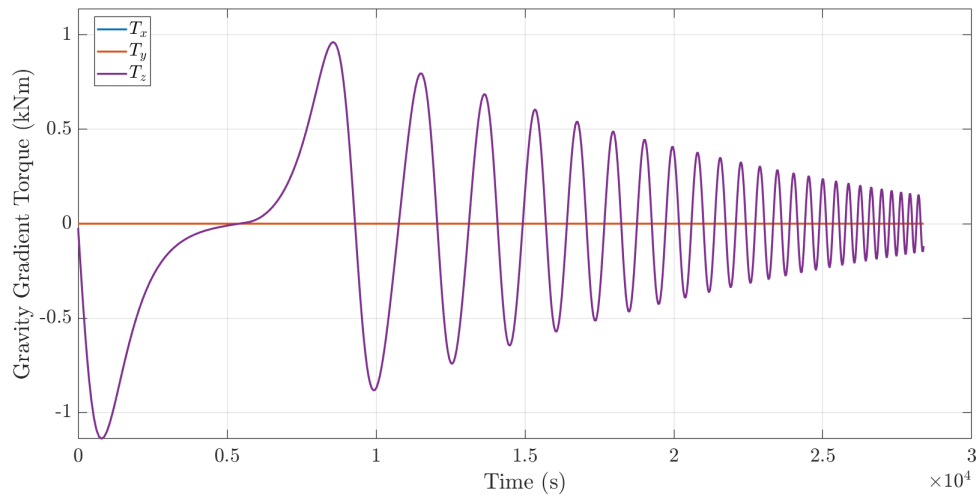

Figure 5.4. Gravity Gradient Torque

Figure 5.5 shows the system attitude quaternion over the maneuver, confirming that the system spin rate increases over time as the tether length decreases. Imparting the initial spin over the first orbit places the TSS in a stable spinning configuration.
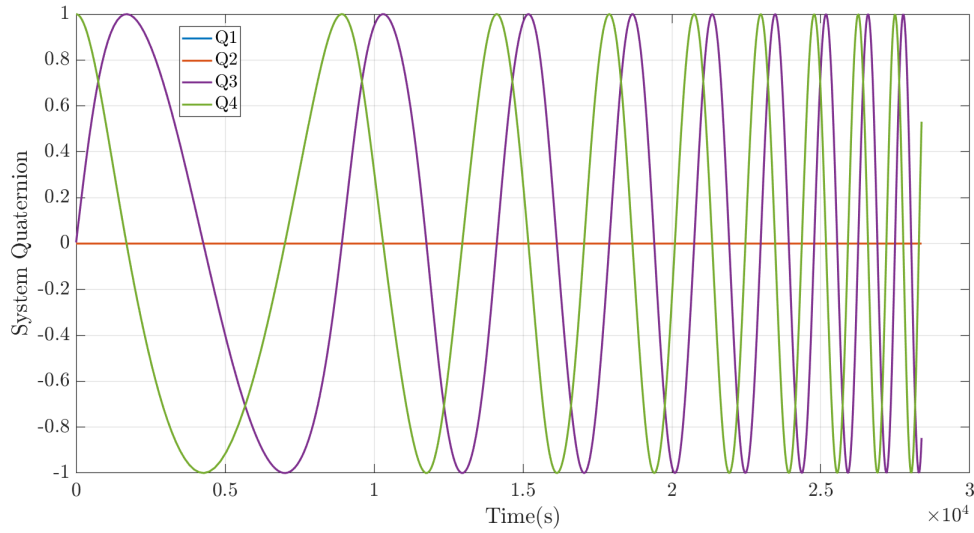
Figure 5.5. Tethered System Attitude Quaternion

In order to conserve momentum, after the tether retrieval begins at the end of the first orbit, the TSS angular velocity, ω must increase. Figure 5.6 shows the increase in pitch rate. Additionally, as ω increases, the amplitude of its oscillation decreases.
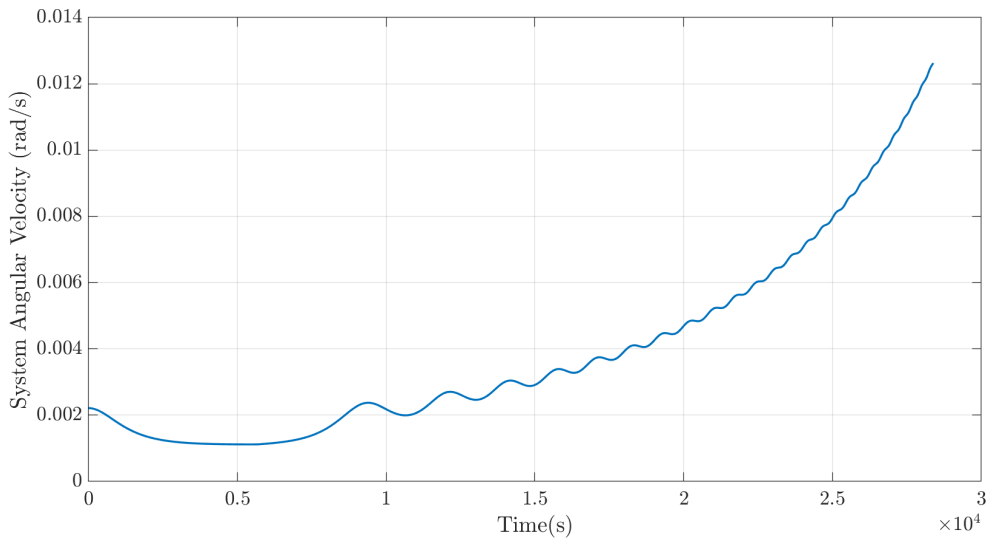

Figure 5.6. Tethered System Angular Velocity

Equations (5.14) and (5.15) indicate that the velocity of each end body at the point of separation (assuming the separation occurs along the local vertical and that β is instantaneously

40

0), can be described as function of pitch rate, $\dot{\beta}$ and the changing tether length. Figure 5.7 displays the effect of increasing pitch rate on the separation velocity. From this, it can be inferred that the SV will experience an orbital change to a much higher orbit, and as the debris speed decreases, the debris object will transfer to a lower orbit, as intended.
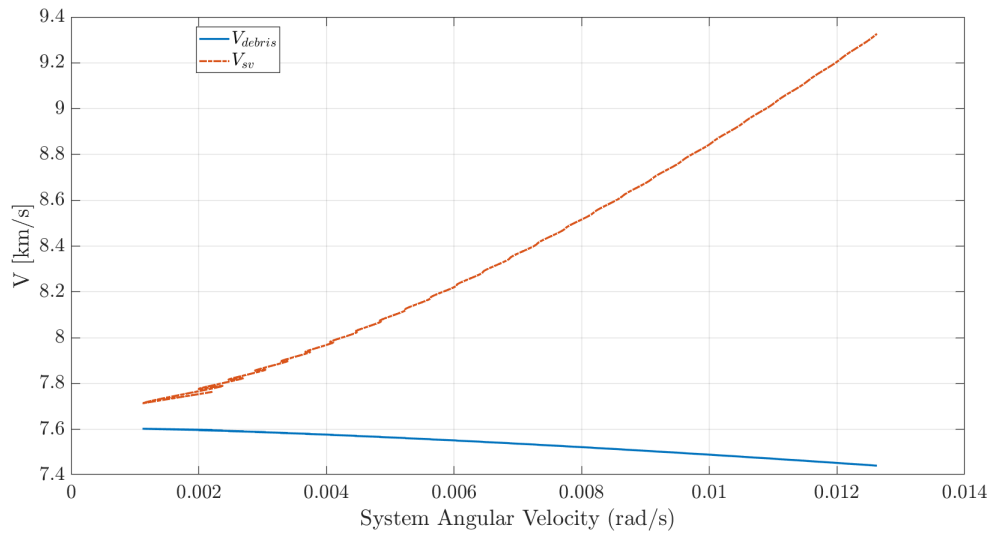

Figure 5.7. Separation Velocities

By calculating the difference between the separation velocity of the debris and its initial circular velocity, the ΔV of the debris can be determined, as shown in Figure 5.8. This figure also compares the ΔV of the debris with the decreasing tether length. As is shown, the debris can attain a ΔV of over 150 m/s over the course of five orbits.

Figure 5.8. ΔV at Separation
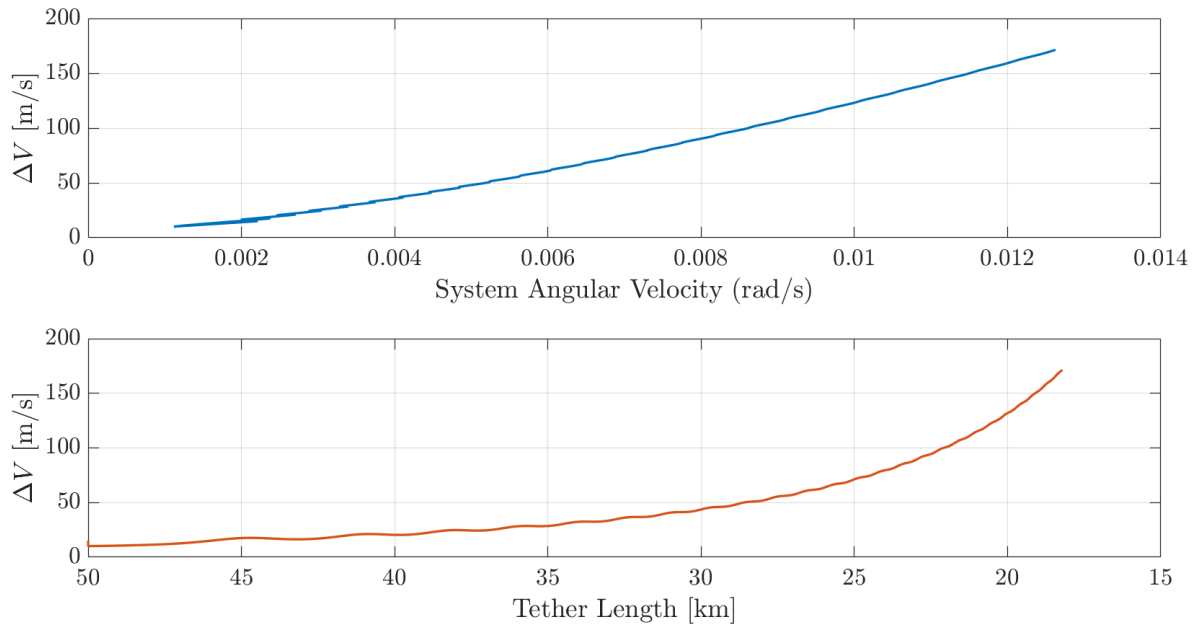
If the debris were released at the end of the system's fifth orbit, Figure 5.8 shows that the debris would experience a ΔV of 171.3783 m/s, well in excess of the necessary 145 m/s.

Therefore, the spin-up momentum-exchange maneuver is a numerically feasible ADR method. Releasing the debris when aligned with the local vertical on a forward spin, imparts positive ΔV to the SV and negative ΔV to the debris, effectively sending the debris on at reentry trajectory, without the use of propellant, save for the impulse required to establish the initial spin rate. Additional simulations show that even with the initial pitch rate of solely the natural frequency of libration, the debris can attain a ΔV of 108.9 m/s, placing the debris into a terminal orbit, if natural orbital decay were permissible. In reentry mission planning, the tether length could be controlled such that the maneuver will impart a ΔV that will establish the preferred reentry trajectory.

CHAPTER 6:
Optimization of Propulsive Deorbit

To compare the results of tethered ADR to more typical ADR methods, a scenario was considered where a debris removal system conducted a propulsive-targeted reentry, instead of a propellant-less tethered momentum exchange seen in Chapter 5. This method sought to optimize a minimum time propulsive reentry of the debris to the "spacecraft cemetery" region of the Pacific Ocean, also known as "Point Nemo" in the vicinity of 45° $52.6'$ S 123° $23.6'$ W. This region is known as the oceanic pole of inaccessibility and has been the terminal destination for over 263 spacecraft since 1971 [45]. As with all other analyses in this thesis, the debris is assumed to have already been captured. Figure 6.1 shows a diagram of this orbital transfer maneuver. The plane shown in the figure represents the orbital plane.
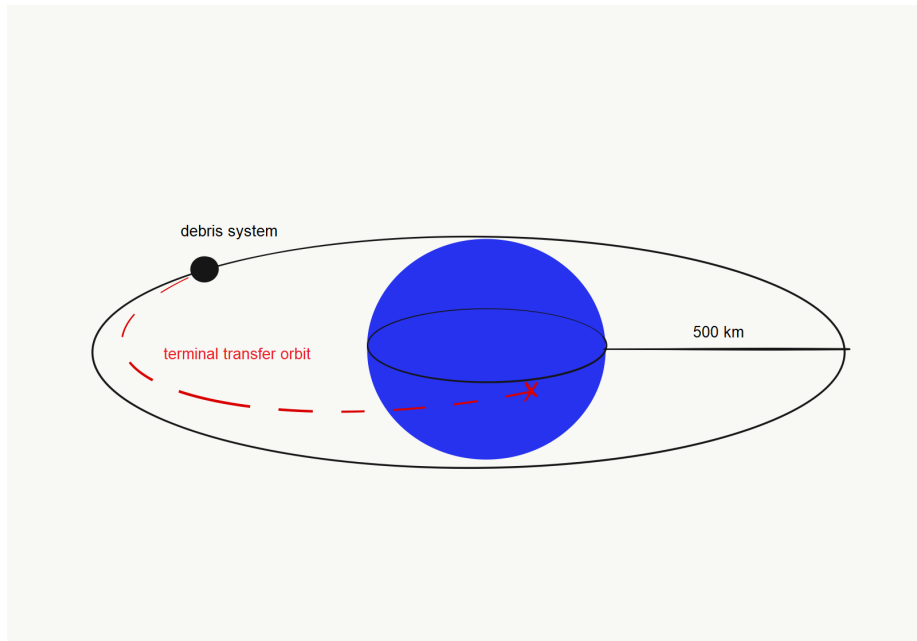

Figure 6.1. Orbital Transfer to Terminal Orbit

This maneuver can be considered a typical Hohmann transfer, with the final orbit having a perigee radius that intersects the surface of the earth, as with the calculations presented in section 5.1. Two thruster configurations were considered for this scenario, a monopropellant

hydrazine thruster, typically known as a Liquid Apogee Engine (LAE), which are often used for orbital transfer maneuvers, and an ion-thruster known as Hall-Effect Thruster, which are often used for orbital insertion and stationkeeping [46].

6.1 Optimization Problem Definition

The unscaled orbit-to-orbit optimal control problem can be described in polar coordinates with the following:

$$\mathbf{X} = [r, \theta, v_r, v_t, m]^T \in \mathcal{R}^5, \qquad\qquad \mathbf{u} = [T, \alpha] \in \mathcal{R}^2$$

$$P:1 \begin{cases} \text{Minimize} & J = \left[x\left(\cdot\right), u\left(\cdot\right), t_f \right] = t_f \\ \text{Subject to:} & \dot{r} = v_r \\ & \dot{\theta} = \frac{v_t}{r} \\ & \dot{v_r} = \frac{v_t^2}{r} - \frac{\mu}{r^2} \\ & \dot{v_t} = -\frac{v_r v_t}{r} \\ & \dot{m} = \frac{T}{v_e} \\ & t_0 = 0 \\ & (r_0, \theta_0, v_{r0}, v_{t0}, m_0) = \left(r^0, 0, 0, \sqrt{\frac{\mu}{r_0}}, m^0 \right) \\ & (r_f) = \left(r^f \right) \end{cases} \qquad (6.1)$$

where the optimization variables are $\mathbf{X}$, the state trajectory, $\mathbf{u}$, the control trajectory, and t_f, the final clock time. The problem formulation in Equation (6.1) assumes that Earth is spherical and effects due to oblateness can be neglected, the deorbiting spacecraft system is a perfect sphere and attitude effects can be ignored, and the initial orbital plane and the terminal orbital plane are co-planar.

6.2 Scaling

Due to the large units of the problem, e.g., thousands of kilometers and hundreds of newtons, best practice suggests scaling and use of canonical units [47]. The scaled canonical units

were determined as follows:

$$\text{length unit } LU = 6878, \qquad\qquad \text{such that } r_0 = 1$$
$$\text{mass unit } MU = 10000, \qquad\qquad \text{such that } m_f = 1$$

and by setting the scaled gravitational parameter $\tilde{\mu}$ equal to 1, the following canonical units can be derived

$$\tilde{\mu} = \frac{TU^2 \mu}{DU^3} \qquad \text{and therefore, time unit } TU = 903.4915$$
$$\text{velocity unit } VU = \frac{LU}{TU} = 7.6127 \qquad \text{Force unit } FU = MU\frac{LU}{TU^2} = 84.2586$$

Table 6.1 contains the unscaled and scaled values for the known constants and boundary conditions of Equation (6.1).

Table 6.1. Scaled Values for Constants and Known Boundary Conditions

	Unit	Unscaled Value	Scaled Value
Orbit altitude	r_0	6878 km	1
	r_f	6378 km	.9273
Velocity	v_{t0}	7.6127 km/s	1
	v_e	2.2563 km/s	0.2964
System Mass	m_0	225000 kg	2.25
	m_f	10000 kg	1
Thrust	F	440 N	5.222
Gravitational Parameter	μ	398601 km^3/s^2	1

After scaling, all units except for the angles are transformed into the *tilde space*. The orbit angle and steering angle parameters do not need to be scaled because $\theta = \tilde{\theta}$ and $\alpha = \tilde{\alpha}$.

6.3   Problem Formulation

The Boundary Value Problem (BVP) for the scaled problem was formulated using conditions from Pontryagin's Principle. The method for developing the BVP with these conditions is defined in [48] and contains the following six steps:

1. Construct the Hamiltonian. The Hamiltonian is defined as $H(\lambda, x, u) = F(x, u) + \lambda^T f(x, u)$, where F is the scalar running cost, λ refers to the system costate vector, and $f(x, u)$ refers to the system dynamics.

$$H(\lambda, x, u) = \lambda_r v_r + \lambda_\theta \frac{v_t}{r} + \lambda_{v_r}\left(-\frac{\mu}{r^2} + \frac{v_t^2}{r} + \frac{T}{m}\sin\alpha\right) + \lambda_{v_t}\left(-\frac{v_r v_t}{r} + \frac{T}{m}\cos\alpha\right) \quad (6.2)$$

2. Minimize the Hamiltonian. For this scenario, both the thrust, T and the angle of thrust α are control parameters, therefore the Hamiltonian must be globally minimized for both. Since the Hamiltonian is a scalar function, the partial derivative with respect to the control can be described as

$$u = \begin{bmatrix} T \\ \alpha \end{bmatrix} \qquad\qquad \frac{\partial H}{\partial \mathbf{u}} \triangleq \begin{bmatrix} \frac{\partial H}{\partial u_1} \\ \frac{\partial H}{\partial u_2} \end{bmatrix} \qquad\qquad (6.3)$$

$$\frac{\partial H}{\partial T} = \lambda_{v_r}\left(\frac{1}{m}\sin\alpha\right) + \lambda_{v_t}\left(\frac{1}{m}\cos\alpha\right) + \lambda_m \frac{1}{v_e} = 0 \qquad (6.4)$$

$$\frac{\partial H}{\partial \alpha} = \lambda_{v_r}\left(\frac{T}{m}\right)\cos\alpha - \lambda_{v_t}\left(\frac{T}{m}\right)\sin\alpha = 0 \qquad (6.5)$$

An expression for the control parameter thrust cannot be derived from minimizing the Hamiltonian from this calculation. The minimization must be done within the constraints of the system thruster via a switching function. An expression for the optimal thruster angle can, however, be derived as follows:

$$\alpha = \tan^{-1}\left(\frac{\lambda_{v_r}}{\lambda_{v_t}}\right) \qquad\qquad (6.6)$$

The Hamiltonian could be minimized on T with the inclusion of a switching structure to create a complementary condition on which T is bounded, or these controls can be bounded in the control search space for the DIDO software. For this reason, DIDO was chosen as the preferred tool to develop this solution.

3. Determine the adjoint equation and define the dynamics of the costates.

$$\frac{\partial H}{\partial \mathbf{x}} = -\dot{\lambda} \tag{6.7}$$

$$\dot{\lambda}_r = \lambda_\theta \frac{v_t}{r^2} - 2 * \lambda_{v_r} \frac{\mu}{r^3} + \lambda_{v_r} \frac{v_t^2}{r^2} - \lambda_{v_t} \frac{v_r * v_t}{r^2} \tag{6.8}$$

$$\dot{\lambda}_\theta = 0 \tag{6.9}$$

$$\dot{\lambda}_{v_r} = -\lambda_r + \lambda_{v_t} \frac{v_t}{r} \tag{6.10}$$

$$\dot{\lambda}_{v_t} = -\frac{\lambda_\theta}{r} - 2 * \lambda_{v_r} \frac{v_t}{r} + \lambda_{v_r} \frac{v_r}{r} \tag{6.11}$$

$$\dot{\lambda}_m = \lambda_{v_r} \frac{T \sin \alpha}{m^2} + \lambda_{v_t} \frac{T \cos \alpha}{m^2} \tag{6.12}$$

4. By defining the system Endpoint Lagrangian, $\bar{E}$, the terminal costates $\lambda(\mathbf{t_f})$ can be determined by taking the gradient of the Endpoint Lagrangian function with respect to the final states $\mathbf{x_f}$. This equation, (6.14), is also known as the terminal transversality condition.

$$\bar{E} = E + v^T \mathbf{e} \tag{6.13}$$

$$\frac{\partial E}{\partial \mathbf{x_f}} = \lambda(t_f) \tag{6.14}$$

$$\frac{\partial E}{\partial r_f} = v_r = \lambda_r(t_f) \tag{6.15}$$

The endpoint condition for r offers no new information, however, the following parameters are left as free parameters, and the final value of each costate can be

47

determined as follows:

$$\lambda_\theta(t_f) = 0 \tag{6.16}$$

$$\lambda_{v_r}(t_f) = 0 \tag{6.17}$$

$$\lambda_{v_t}(t_f) = 0 \tag{6.18}$$

$$\lambda_m(t_f) = 0 \tag{6.19}$$

$$\tag{6.20}$$

5. The Hamiltonian Value Condition also provides insight into the unknown boundary conditions. The gradient of the Endpoint Lagrangian with respect to the final time indicates the final value of the Hamiltonian.

$$H[@t_f] = -\frac{\partial \bar{E}}{\partial t_f} = 1 \tag{6.21}$$

$$-\frac{\partial \bar{E}}{\partial t_f} = 1 \rightarrow \frac{\partial \bar{E}}{\partial t_f} = -1 \tag{6.22}$$

6. The Hamiltonian Evolution Equation indicates that the Hamiltonian does not depend on time and the minimized Hamiltonian is equal to -1. The plot of the Hamiltonian should be a constant value at -1.

$$\frac{d\mathcal{H}}{dt} = \frac{\partial H}{\partial t} = 0 \tag{6.23}$$

6.4 Simulation Results

During troubleshooting efforts, θ_f was released to be a free parameter out of concerns that it was over-constraining the problem. With this in mind, as with the other free parameters, the final costate should equal 0.

6.4.1 LAE Thruster Results

Figure 6.2 shows the unscaled states and costates of the solution using the LAE. As can be seen by the costate plot, the final costates for $\lambda_\theta, \lambda_{v_r}, \lambda_{v_t}$, and λ_m are all 0, which verifies the transversality condition for these four free parameters.
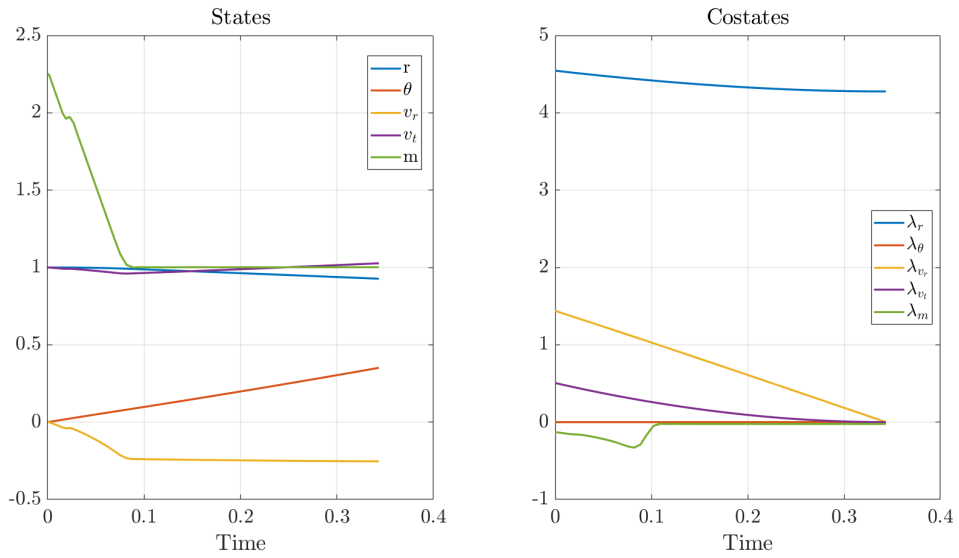
Figure 6.2. Unscaled States and Costates

Figure 6.3 shows the unscaled system trajectory and that the system deorbits from an initial altitude of 500 km to a final altitude of 0, effectively impacting the Earth's surface (not accounting for drag effects).
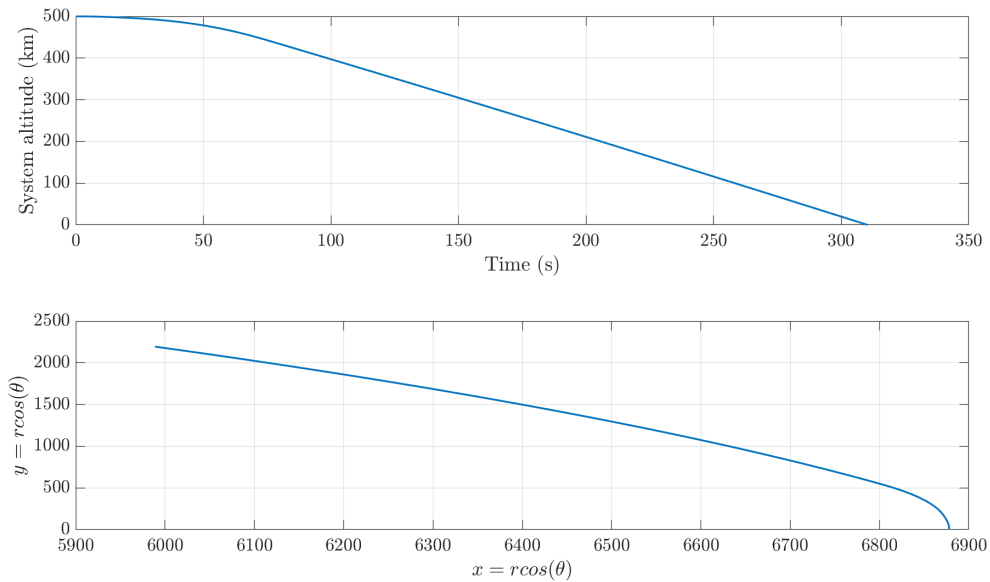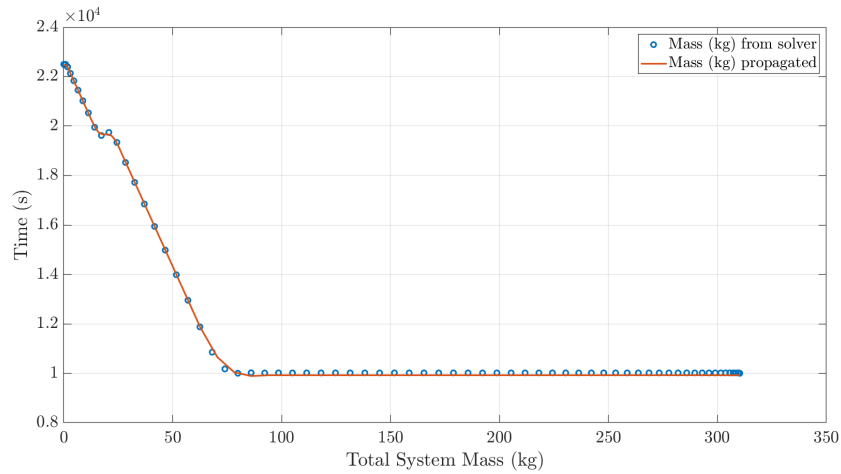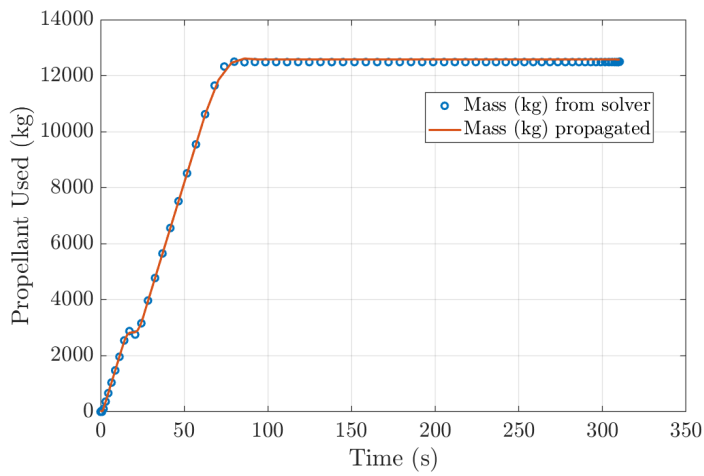

Figure 6.3. System Trajectory

49

(a) Total System Mass

(b) Propellant Used

Figure 6.4. System Mass and Propellant Used with LAE

The initial problem formulation only accounted for an additional 1000 kg of fuel to be added to the 10,000 kg system. However, this did not result in a feasible solution. Much trial and error resulted in ultimately increasing the initial mass of the system by 12,500 kg to find a feasible solution. The feasibility of the solution was determined via feasibility analysis and by observing the effects on the Hamiltonian evolution. The resulting initial mass for a satisfyingly constant Hamiltonian was 22,500 kg. Figure 6.4 suggests that to perform this minimum time deorbit maneuver, the system operates at a high thrust, expending all of its fuel within the first 80 seconds.

Figure 6.5 measures the control effort of the system and complements the propellant usage plot. The system appears to operate at nearly constant maximum thrust until the propellant is expended. Initially the bounds for thrust were between the maximum and minimum capabilities of the thruster, 440N and 130N, respectively [46], which did not allow for the thruster to not operate. Once the minimum bound for thrust was set to 0 N, indicating that the thruster was off, a solution could be found. This control effort could be refined with a switching control method allowing the system to operate between maximum and minimum thrust, or to not operate.
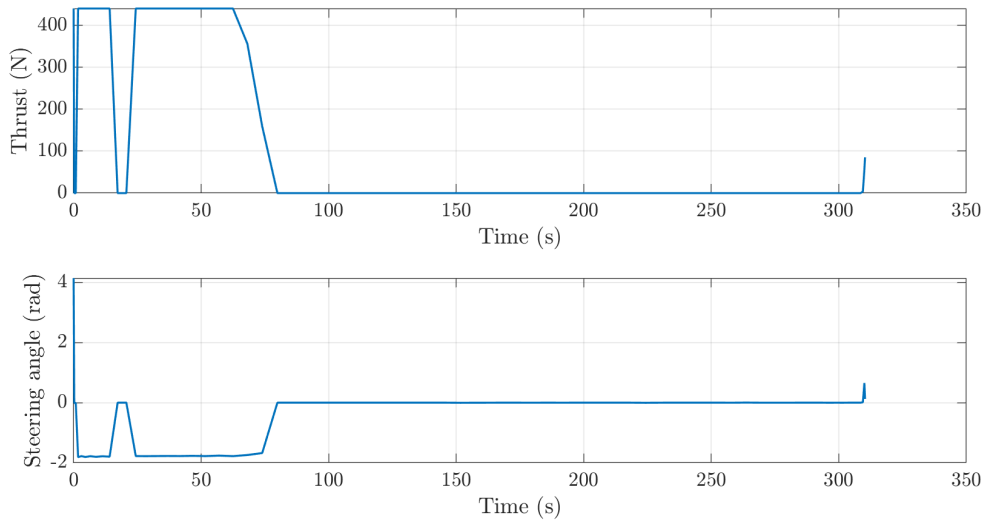

Figure 6.5. System Control Effort - Thrust and Steering Angle

Figure 6.6 shows a relatively constant Hamiltonian plot at -1, which verifies the Hamiltonian Evolution of the problem formulation.
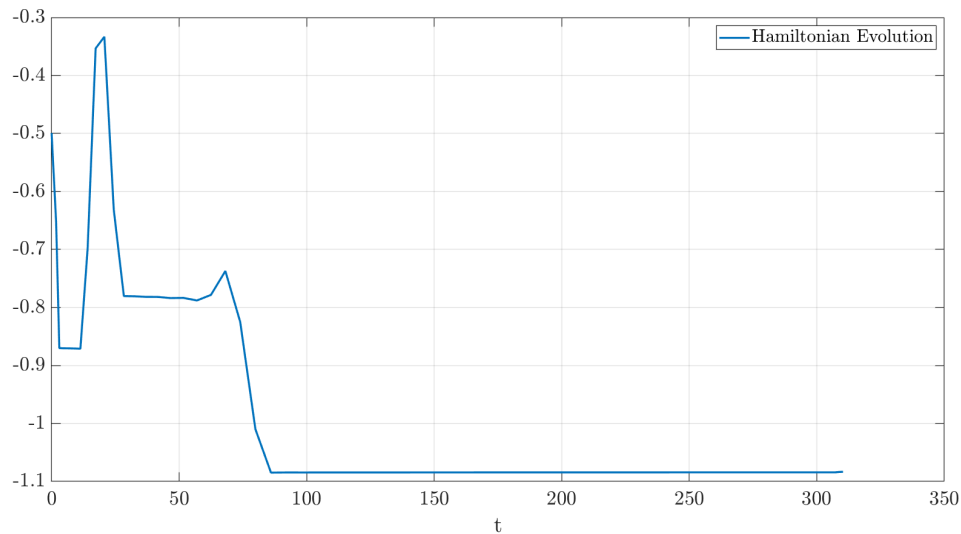

Figure 6.6. Hamiltonian Evolution

LAE Thruster Conclusion

The minimum time maneuver was completed and determined that a 10,000 kg spacecraft orbiting at 500 km altitude can be deorbited in 310.2705 seconds with a Liquid Apogee Engine thruster. However, to do so would require and additional 12,500 kg of fuel! To develop a solution in DIDO, the search space needs to be sufficiently large to find the solution. If the search space was too narrow, the result would be an infeasible solution. Given the large size of the engineering units used to develop this problem, the search space needed to have the necessary breadth.

6.4.2   Hall-Effect Thruster Results

Given the incredible impracticality of implementing the results using the LAE, an additional simulation was run for Equation (6.1) using the control parameters of a Hall-Effect thruster. Hall-Effect thrusters are commonly used ion thrusters that use an electric field to accelerate their propellant (typically Xenon), instead of propellant ignition or cold gas expulsion [46]. The thrust of a Hall-Effect thruster is therefore dependent on power output, electric propellant, and can have exhaust speeds up to 20 km/s. The thruster chosen for this maneuver

has a maximum thrust of 311 mN and an Isp of 2000 s [46]. Figures 6.7 to 6.10 provide a summary of the results with the Hall-Effect thruster.

Figure 6.7 shows the trajectory of the deorbit maneuver. Unlike the LAE solution, this solution takes 9037 s (or 1.592 orbits) to reach its terminal conditions. This is a more reasonable maneuver estimate.
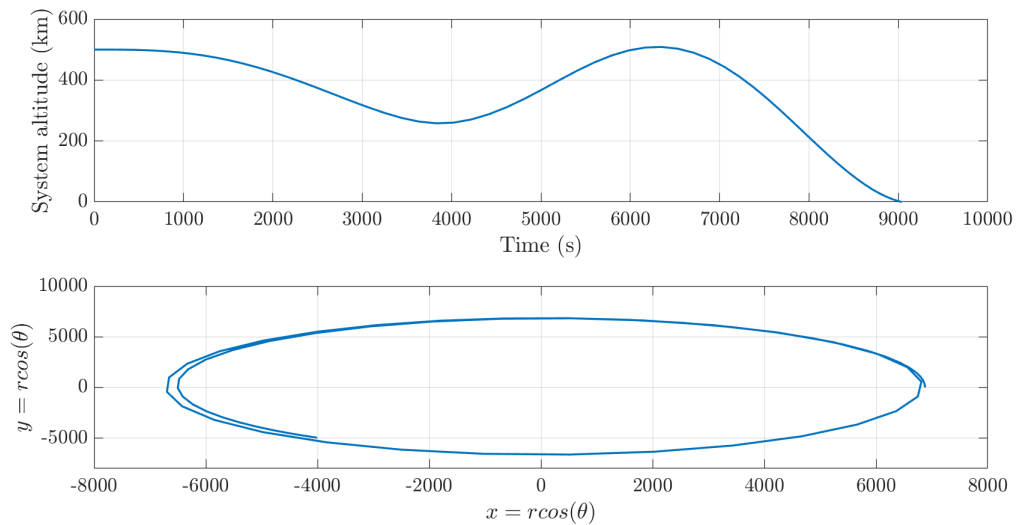

Figure 6.7. System Trajectory Using Hall-Effect Thruster

Figure 6.8 shows the scaled states and costates of the solution. The solution to the BVP presented in Equation (6.1) can be verified by ensuring that the endpoint costates are equal to those defined in the problem formulation.
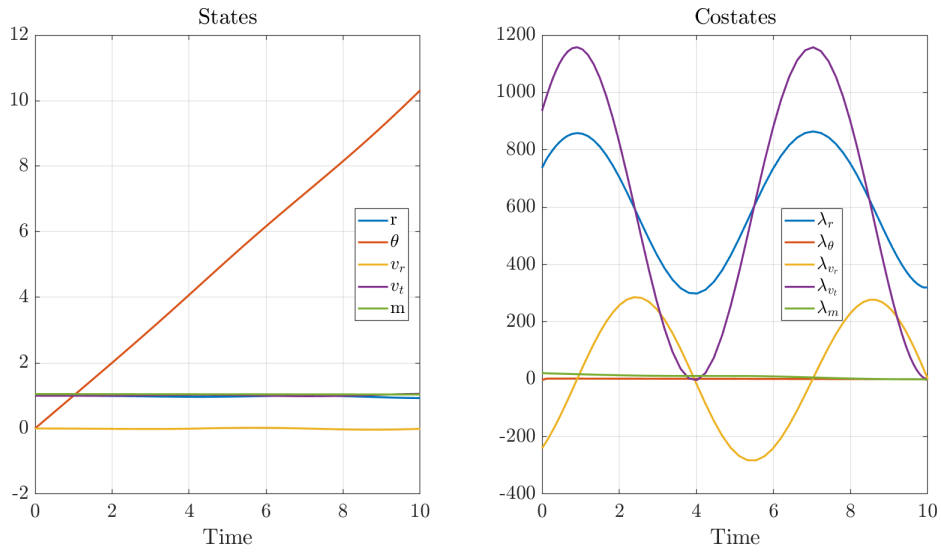
Figure 6.8. Scaled States and Costates Using Hall-Effect Thruster

As shown in Figure 6.9, the Hall-Effect Thruster can complete the minimum time deorbit with an additional 127.7431 kg of propellant.
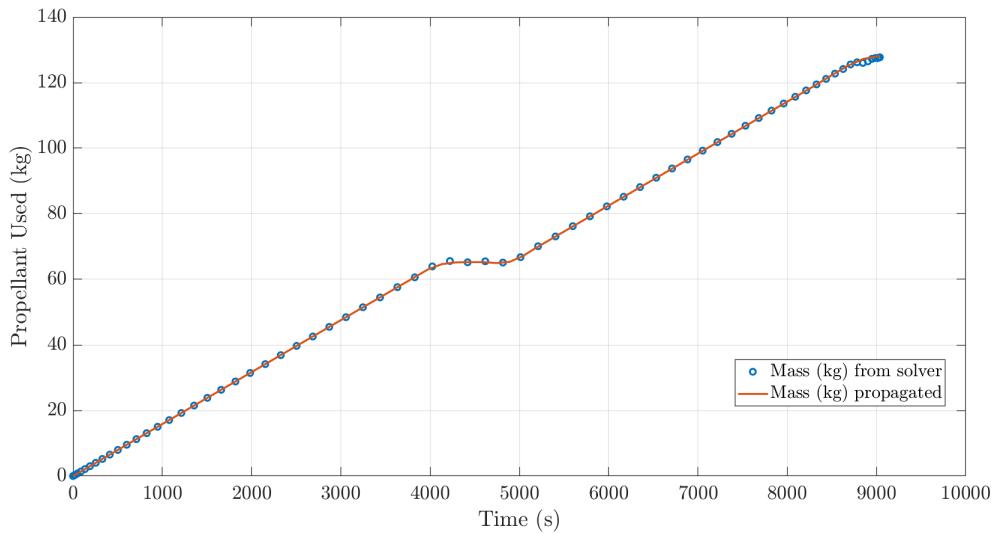

Figure 6.9. Mass of Propellant Used in Maneuver Using Hall-Effect Thruster

Figure 6.10 shows that the system operates at nearly constant maximum thrust throughout the entirety of its deorbit.
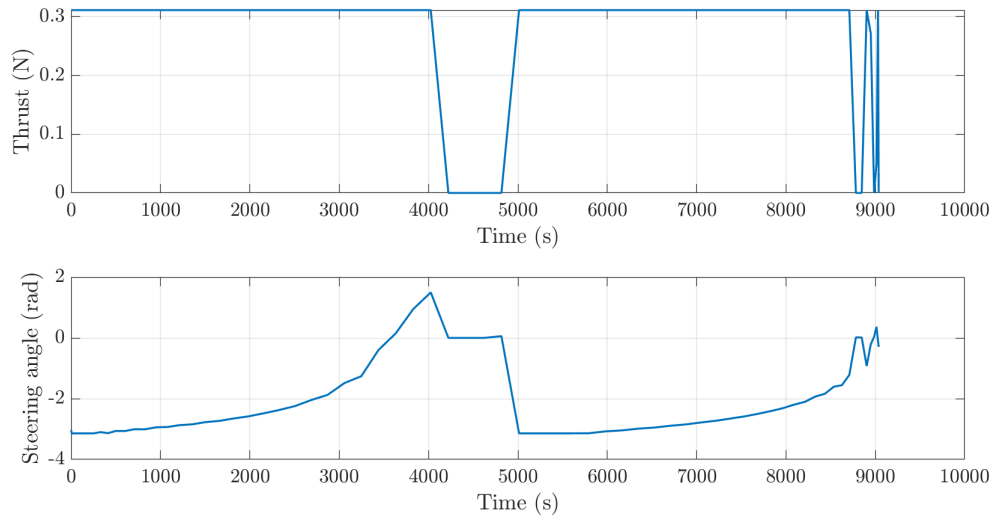
Figure 6.10. Control Effort for Min-Time Maneuver with Hall-Effect Thruster

To develop a feasible solution for both methods, a small running cost had to be included, imposing a penalty on steering angle α to eliminate chatter in the control effort. Were this solution to be implemented on a system, the start point of the maneuver would have to be chosen in the mission design to meet the final intended longitudinal position. The results from the simulation using the Hall-effect thruster suggest that it offers a more realistic option for a minimum time deorbit maneuver than the LAE. This solution could be further refined by introducing a switching control method for the thrust control.

THIS PAGE INTENTIONALLY LEFT BLANK

CHAPTER 7:
Conclusion and Recommendations

7.1 Summary of Findings

This study investigated the need for active debris removal in order to preserve the utility of the LEO Environment. Tethered systems offer a propellantless, reusable method for ADR via a momentum exchange spin up maneuver. STELA was used to validate the debris candidacy for removal, and the rigid body tether dumbbell model was evaluated for the maneuver.

The results of the simulation, developed in MATLAB and Simulink, showed that by decreasing the tether length, and spinning up the TSS, a ΔV could be reached to effectively send the debris on a terminal trajectory. The tether retrieval rate can be controlled to ensure that the system attains the desired deorbit velocity. Chapter 6 showed that a propulsive deorbit method can be optimized for minimum time. Propulsive methods can be quick and reliable, but require additional fuel and may only be practical for specific propulsive systems, which limits the missions to which it may be applicable. Additionally, a propulsive deorbit system would be single-use only and would be an incredibly expensive ADR method. A tethered solution can be applicable across many mission as long as the debris is able to be captured.

7.2 Recommendations for Future Work

As the field of active debris removal is a relatively new area of application for space technologies, there are many directions that future work could explore.

The momentum exchange maneuver presented in Chapter 5 can be expanded by developing a more robust control law for the tether retrieval mechanism to account for librational oscillations that may be caused during the retrieval. Additionally, a mission plan could be developed to use SV's ΔV to rendezvous with an additional debris to perform the deorbit spin maneuver, to further the studies seen in [16] and [42]. In a physical system, it is more likely that the tether will have elastic properties, which have been ignored here. The next step for this comparison could be to conduct the same analyses but simulating an elastic

tether instead of a rigid one, or to conduct the analysis along an elliptical orbit. The non-rigid tether model will also vary based on the tether physical properties, which is subject to material and structural analysis.

While the typical tethered configuration for a system is aligned for to librate around the local vertical, as seen in Chapter 5, a towing system would typically experience a continuous low force and have a closer alignment with the local horizontal. Due to this configuration, the dynamics of this system and natural librational frequencies must be calculated differently [49]. A future application of this tethered research could be to evaluate the dynamics of this configuration, and exploit the atmospheric drag force with a drag augmentation device for another propellantless solution, instead of the typically studied propulsive space tug.

Another future application of this work could be to take the optimized deorbit demonstrated in Chapter 6 and include the tethered system dynamics or to refine the control method.

APPENDIX A:
Comparison of Formation Flying Propagation Methods

A.1   Relative Motion Models

This Appendix compares three different methods for propagating the relative motion between a chief and deputy satellite in proximity flight. This first is the state transition method of solving the Clohessy-Wiltshire equations of motion which are applicable to a chief on a circular orbit and a deputy that is circular, or slightly elliptical and inclined. The second method is the Yamanaka-Ankersen method of solving the Tschauner-Hempel linearized equations of relative motion for an arbitrarily elliptical orbit. The final method performs a numerical integration method to solve the Kepler equations of motion for each orbit, then determines the relative motion between them.

For each method, the orbital elements were defined as presented in Tables A.1 and A.2.

Table A.1. Orbital Elements with Chief on Circular Orbit

Orbital Elements	Chief	Deputy
a, semi-major axis [km]	8500	8500.1
e, eccentricity	0	0.01
i, inclination [deg]	15	15.5
Ω, RAAN [deg]	30	30
ω, argument of perigee [deg]	10	10
ν, true anomaly [deg]	0	0

Table A.2. Orbital Elements with Chief on Elliptical Orbit

Orbital Elements	Chief	Deputy
a, semi-major axis [km]	8500	8500.1
e, eccentricity	0.01	0.02
i, inclination [deg]	15	15.5
Ω, RAAN [deg]	30	30
ω, argument of perigee [deg]	10	10
ν, true anomaly [deg]	0	0

A.1.1 Clohessy-Wiltshire Equations of Relative Motion

The Clohessy-Wiltshire (CW) equations presented in Equations (4.21) to (4.23) can describe the relative motion relative motion when the chief satellite is in a circular orbit, the deputy is only slightly elliptic and inclined compared to the chief orbit. The relative motion equations are linearized about the origin of the chief-fixed LVLH frame. [28] The linear differential equations can be represented in state-space form where the state vector is $\mathbf{x} = [x, y, z, \dot{x}, \dot{y}, \dot{z}]^T$ and the state-space representation assumes the form

$$\dot{\mathbf{x}}(t) = A\mathbf{x}(t)$$

where A is the system matrix:

$$A = \begin{bmatrix} 0 & 0 & 0 & 0 & 1 & 0 & 0 \\ 0 & 0 & 0 & 0 & 0 & 1 & 0 \\ 0 & 0 & 0 & 0 & 0 & 0 & 1 \\ 3n^2 & 0 & 0 & 0 & 0 & 2n & 0 \\ 0 & 0 & 0 & 0 & -2n & 0 & 0 \\ 0 & 0 & 0 & -n^2 & 1 & 0 & 0 \end{bmatrix} \tag{A.1}$$

The solutions to the relative position and velocity components are as follows:

$$x(t) = [4 - 3\cos(nt)]x(0) + \frac{\sin(nt)}{n}\dot{x}(0) + \left[\frac{2}{n} - \frac{2\cos(nt)}{n}\right]\dot{y}(0) \tag{A.2}$$

$$y(t) = [-6nt - 3\sin(nt)]x(0) + y(0) + \left[-\frac{2}{n} + \frac{2\cos(nt)}{n}\right]\dot{x}(0)\left[\frac{4\sin(nt)}{n} - 3t\right]\dot{y}(0) \tag{A.3}$$

$$z(t) = \cos(nt)z(0) + \frac{\sin(nt)}{n}\dot{z}(0) \tag{A.4}$$

$$\dot{x}(t) = 2n\sin(nt)x(0) + \cos(nt)\dot{x}(0) + 2\sin(nt)\dot{y}(0) \tag{A.5}$$

$$\dot{y}(t) = [-6n - 3n\cos(nt)]x(0) + -2\sin(nt)\dot{x}(0) + [-3 + 4\cos(nt)]\dot{y}(0) \tag{A.6}$$

$$\dot{z}(t) = -n\sin(nt)z(0) + \cos(nt)\dot{z}(0) \tag{A.7}$$

where *nt* is the mean anomaly of the chief. The state-space model was solved using a Runge-Kutta numerical integration method. The solution can be seen in Figure A.1.
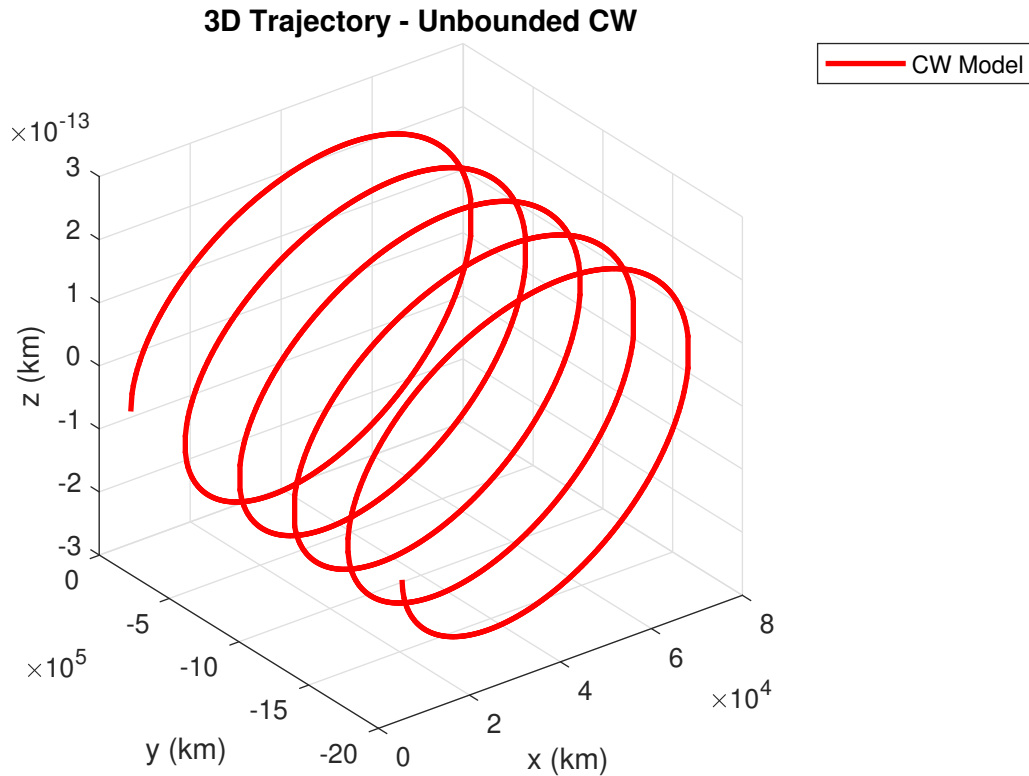

Figure A.1. Unbounded CW

The along-track or y-component of the solution shows the presence of linearly increasing drift due to the $3t$ term in the y-component of the solution. This results in unstable in-plane motion. A *stable subspace* can be found by defining the initial condition

$$\dot{y}(0) = -2nx(0)$$

and bounding the relative motion to first order [28]. The bounded solution of relative motion is shown in Figure A.2. It is worth noting that stability in the context of CW is local only and is applicable only in the small neighborhood of the chief, and not the relative motion of the formation overall.
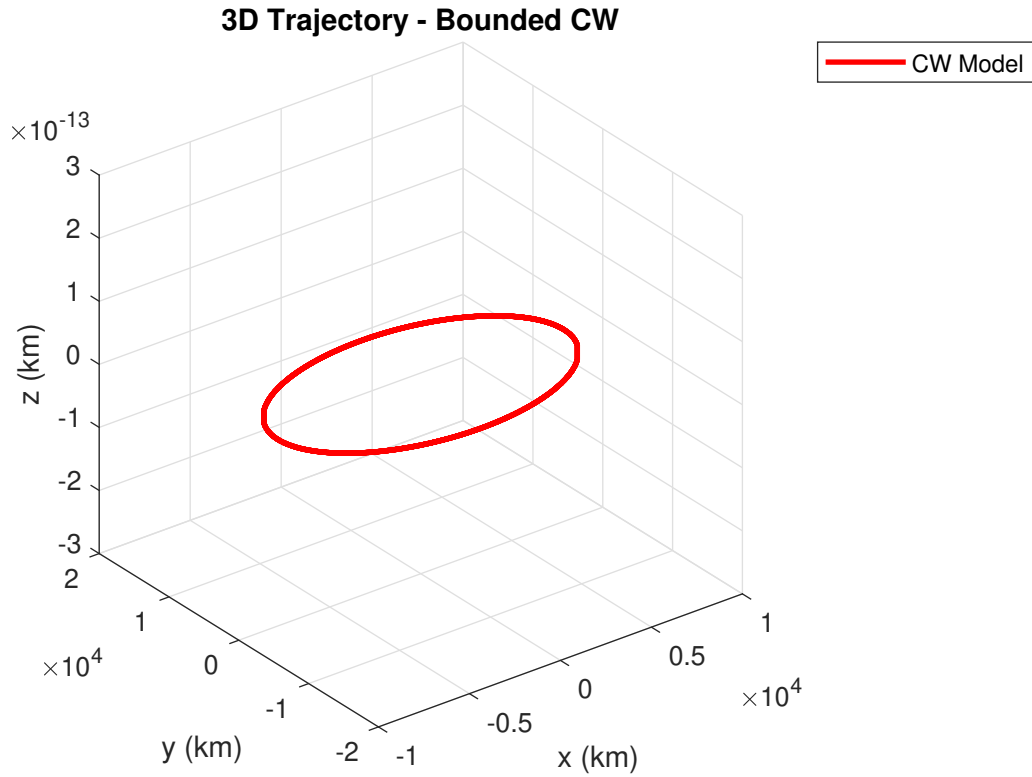
Figure A.2. Bounded CW

A.1.2 Yamanaka-Ankersen method to solve Tschauner-Hempel Equations of Motion

In 2002, Yamanaka and Ankersen developed a state transition matrix for solving arbitrarily elliptical orbits, using true anomaly as the independent variable. The equations of relative motion with true anomaly as the independent vector are known as the Tschauner-Hempel Equations:

$$\tilde{x}'' = \frac{3\tilde{x}}{\rho(\nu)} + 2\tilde{y}' \tag{A.8}$$

$$\tilde{y}'' = -2\tilde{x}' \tag{A.9}$$

$$\tilde{z}'' = -\tilde{z} \tag{A.10}$$

where $\rho(v)$ is $1 + e\cos(v)$. To solve these relative motion equations, the state vector must be transformed into the tilde space using the following method presented [50].

$$[\tilde{x}, \tilde{y}, \tilde{z}, \tilde{x}', \tilde{y}', \tilde{z}']^T = A(v)[x, y, z, \dot{x}, \dot{y}, \dot{z}]^T \tag{A.11}$$

$A(v)$ is the matrix:

$$A(v) = \begin{bmatrix} k * \rho * \mathbf{I}_{3x3} & 0_{3x3} \\ -k * e * \sin(v) * \mathbf{I}_{3x3} & \frac{1}{k*\rho} * \mathbf{I}_{3x3} \end{bmatrix} \tag{A.12}$$

where $k = \sqrt{\frac{h}{p^2}}$. The complete solution to the Tschauner-Hempel equations using the Yamanaka-Ankersen method is

$$\mathbf{x}(t) = \Phi(v)\Phi^{-1}(v(0))\mathbf{x}(t_0) \tag{A.13}$$

where the solution matrix is

$$\Phi = \begin{bmatrix} s & c & 2 - 3esJ & 0 & 0 & 0 \\ c\left(1 + \frac{1}{\rho}\right) & -s\left(1 + \frac{1}{\rho}\right) & -3\rho^2 J & 1 & 0 & 0 \\ 0 & 0 & 0 & 0 & \cos v & \sin v \\ s' & c' & -3es'J + \frac{s}{\rho^2} & 0 & 0 & 0 \\ -2s & e - 2c & -3(1 - 2esJ) & 0 & 0 & 0 \\ 0 & 0 & 0 & 0 & -\sin v & \cos v \end{bmatrix} \tag{A.14}$$

where $c = \rho\cos(v)$, $s = \rho\sin(v)$ and J is the integral term $J = k^2(t - t_0)$. [33] The solution to the relative position components are

$$x = c_1 k \sin v + c_2 \rho \cos v + c_3(2 - 3e\rho J \sin v) \tag{A.15}$$

$$y = c_4 + c_1(1 + 1/\rho)\cos v - c_2(1 + 1/\rho)\sin v - 3c_3\rho^2 J \tag{A.16}$$

$$z = c_5 \cos v + c_6 \sin v \tag{A.17}$$

When the eccentricity of the chief's orbit is circular, the $\rho(v)$ is 1, and the solution is identical to that of the CW propagation, as seen in Figure A.3.
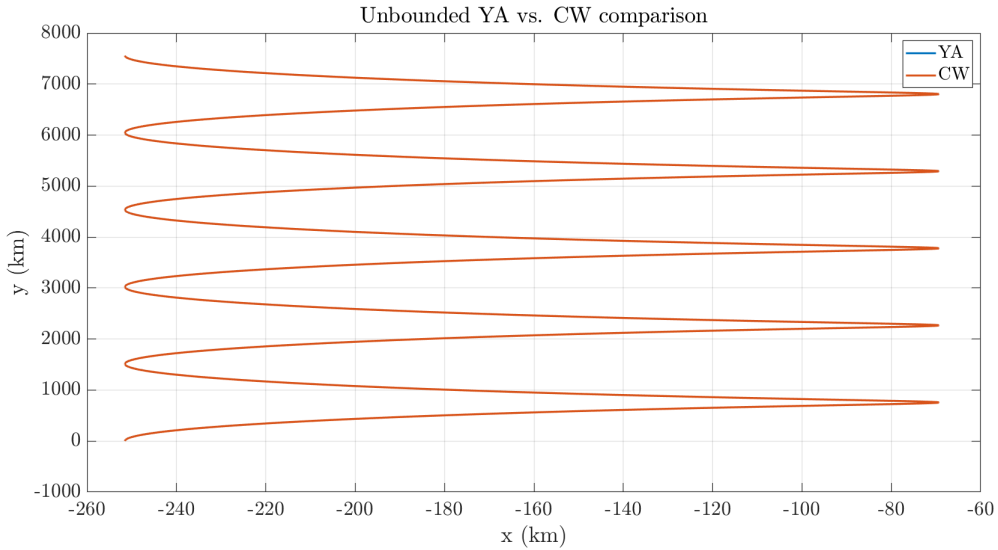
63

Figure A.3. In-Plane Motion for Chief in Circular Orbit

Similarly to Clohessy-Wiltshire, the Yamanaka-Ankersen propagation experiences linearly increasing secular drift due to the presence of the time term in J in the solution. The YA solution can be bounded by setting the appropriate integration constant, c_3 to 0.

A.2 Comparison of Relative Motion Models

The numerical solution was found by integrating the Keplerian equations of motion for both the chief and the deputy satellite using Runge-Kutta-Fehlberg numerical integration methods. The resulting state vector of the deputy was then subtracted from the chief to find the relative motion vector, and converted into the LVLH frame at each time step of the orbit. The intention of including this method was to compare the CW and Yamanaka-Ankersen approximations to the actual numerical solution.

The solution for both the chief and deputy's Keplerian orbit is shown in Figure A.4. As can be seen by the red line representing the deputy's orbit, the deputy is slightly elliptical and slightly inclined compared to the chief.
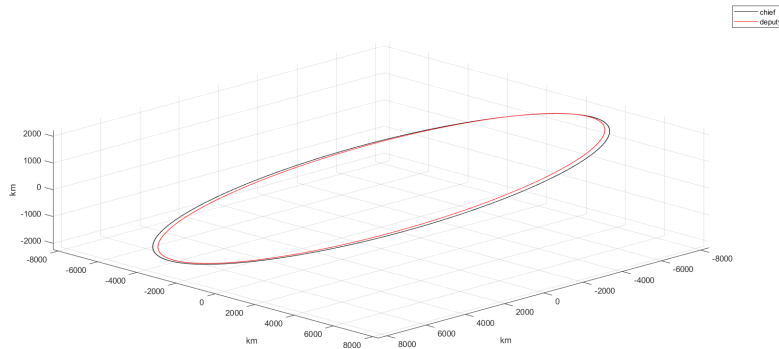
Figure A.4. Numerical Solution Chief in Circular Orbit

Figure A.5 displays the propagation of each solution concurrently for comparison. As previously stated, when the chief is circular, the CW and Yamanaka-Ankersen solutions are identical. As can be seen by the plot, the two approximations can effectively approximate the shape of the numerical relative motion plot, however not without some errors as the plot appears to be shifted along the x direction.
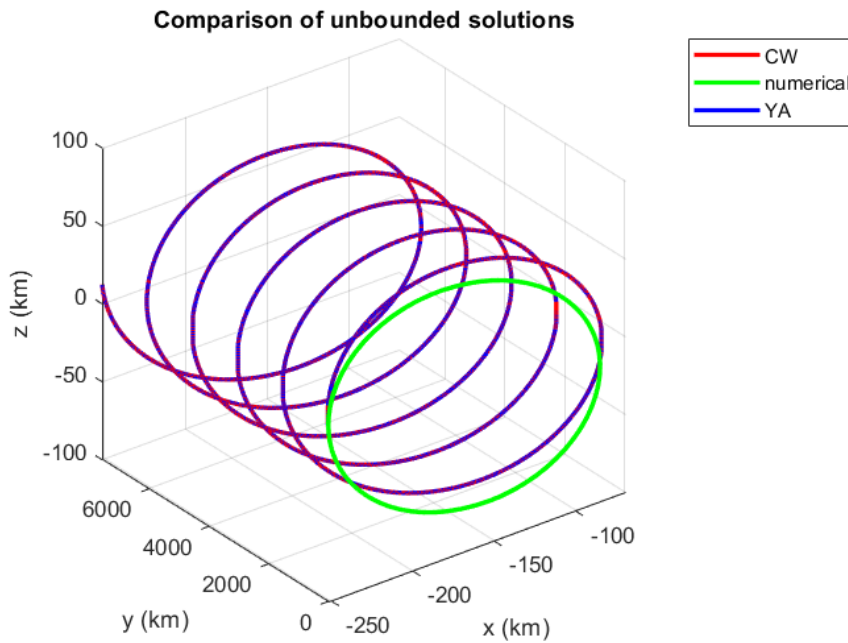

Figure A.5. Unbound Solution Chief in Circular Orbit

The numerical solution for both the chief and deputy's Keplerian orbit, where the chief is in a slightly elliptic orbit, is shown in Figure A.6. The deputy orbit eccentricity has also been slightly increased to maintain a notable orbital separation.
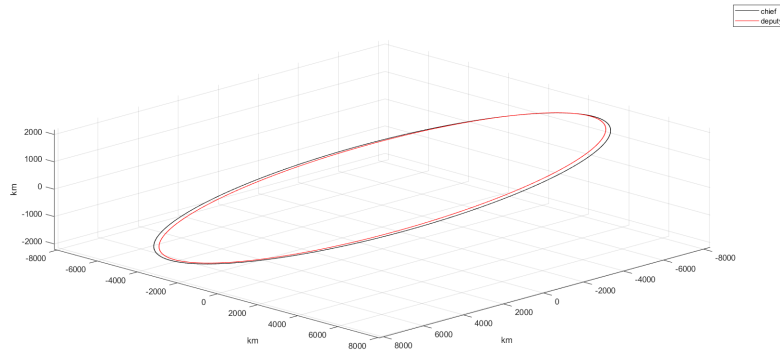

Figure A.6. Numerical Solution Chief in Eccentric Orbit

In Figure A.7, the benefits of the Yamanaka-Ankersen method over the CW method can be clearly seen. Even with slight eccentricity in the chief's orbit, the CW approximation shows significant errors as that solution matrix does not take account of the eccentricity element. The Yamanaka-Ankersen solution degrades dramatically as the solution propagates, however, as with Figure A.5, the initial approximation matches that of the numerical solution, albeit shifted.
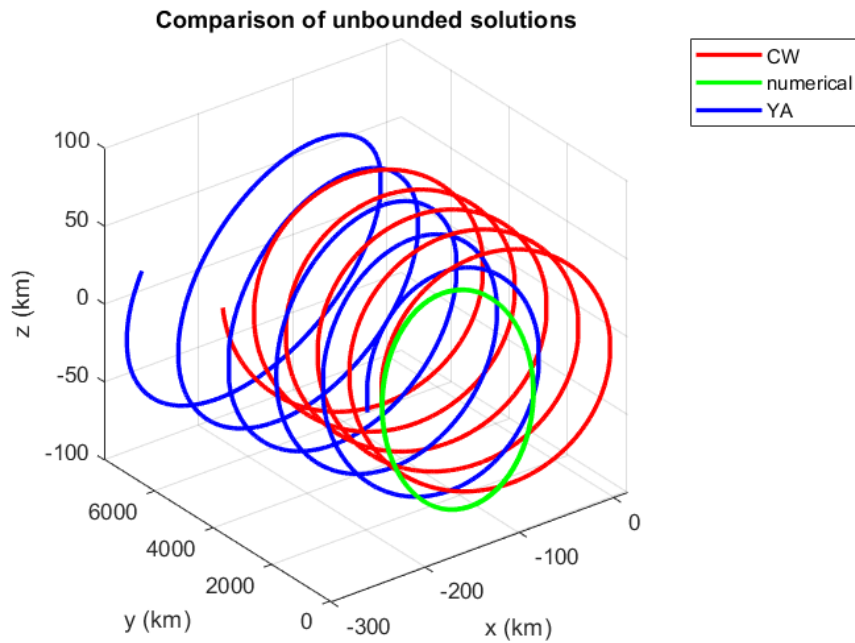
Figure A.7. Unbound Solution Chief in Eccentric Orbit

The CW equations and YA methods offer an approximation to the relative motion problem. However, the accuracy of the solution degrades as the approximation propagates over time [30]. Therefore, it can be reasonably seen why these methods are typically utilized for short term rendezvous scenarios.

THIS PAGE INTENTIONALLY LEFT BLANK

List of References

[1] *Orbital debris management & risk mitigation*. NASA Academy of Program/Project and Engineering Leadership, 2012.

[2] J.-C. Liou, M. Matney, A. Vavrin, A. Manis, and D. Gates, "NASA ODPO's large constellation study," *Orbital Debris News Quarterly*, vol. 22, no. 3, 2018.

[3] J.-C. Liou, N. L. Johnson, and N. M. Hill, "Controlling the growth of future LEO debris populations with active debris removal," *Acta Astronautica*, vol. 66, no. 5-6, pp. 648–653, Mar 2010.

[4] J.-C. Liou, "Orbital debris and future environment remediation," in *OCT Technical Seminar*, 2011.

[5] Treaty on Principles Governing the Activities of States in the Exploration and Use of Outer Space, including the Moon and Other Celestial Bodies. (1967). [Online]. Available: http://www.unoosa.org/oosa/en/ourwork/spacelaw/treaties/outerspacetreaty.html

[6] M. Sorge and G. Peterson, "How to clean space: Disposal and active debris removal," *Crosslinks*, Fall 2015.

[7] U.S. Government Orbital Debris Mitigation Standard Practices. (2001). NASA and DoD Working Group. [Online]. Available: https://orbitaldebris.jsc.nasa.gov/mitigation/

[8] G. Byrne, "NASA orbital debris environment remediation strategies," private communication, Oct. 2018.

[9] "Net successfully snares space debris," University of Surrey, Sep. 2018. Available: https://www.surrey.ac.uk/news/net-successfully-snares-space-debris

[10] Earth observation portal. [Online]. Available: https://directory.eoportal.org/web/eoportal/satellite-missions/r/removedebris

[11] B. Chaudhary, "Unconventional methods for space debris removal," in *Space Safety is No Accident*, T. Sgobba and I. Rongier, Eds. Cham: Springer International Publishing, 2015, pp. 49–58.

[12] E.deorbit: It is time to make active debris removal a reality for the European space sector. (2017, Jan.). ESA. [Online]. Available: http://blogs.esa.int/cleanspace/2017/01/30/e-deorbit-it-is-time-to-make-active-debris-removal-a-reality-for-the-european-space-sector/

[13] Cleanspace one. (2016). EPFL Space Center. [Online]. Available: https://espace. epfl.ch/CleanSpaceOne_1

[14] H. Schaub and D. F. Moorer, "Geosynchronous large debris reorbiter: challenges and prospects," *The Journal of the Astronautical Sciences*, vol. 59, no. 1-2, pp. 161–176, jun 2012.

[15] J. R. Sanmartín, A. Sánchez-Torres, S. B. Khan, G. Sánchez-Arriaga, and M. Charro, "Optimum sizing of bare-tape tethers for de-orbiting satellites at end of mission," *Advances in Space Research*, vol. 56, no. 7, pp. 1485–1492, Oct 2015.

[16] J. Missel and D. Mortari, "Sling satellite for debris removal with Aggie sweeper," Feb. 2011, presented at AAS/AIAA 21st Space Flight Mechanics Meeting in New Orleans, LA.

[17] DARPA. (2018, Aug.). Robotic payload for RSGS mission moves to next phase of development. [Online]. Available: https://www.darpa.mil/news-events/2018-08-17

[18] V. V. Beletsky and E. M. Levin, *Dynamics of space tether systems* (Advances in the Astronautical Sciences). American Astronautical Society, 1993, vol. 83.

[19] K. D. Kumar, "Review of dynamics and control of nonelectrodynamic tethered satellite systems," *Journal of Spacecraft and Robotics*, 2006.

[20] Y. Chen, R. Huang, X. Ren, L. He, and Y. He, "History of the tether concept and tether missions: A review," *ISRN Astronomy and Astrophysics*, vol. 2013, pp. 1–7, 2013.

[21] NASA Space Science Data Coordinated Archive. Gemini-11. NSSDCA/COSPAR ID: 1966-081A. [Online]. Available: https://nssdc.gsfc.nasa.gov/nmc/masterCatalog. do?sc=1966-081A. Accessed Aug. 16 2018.

[22] M. V. Pelt, *Space tethers and space elevators*. Berlin, Germany: Springer, 2009.

[23] M. Dobrowolny and N. H. Stone, "A technical overview of TSS-1: the first tethered-satellite system mission," *Il Nuovo Cimento C*, vol. 17, no. 1, pp. 1–12, Jan 1994.

[24] D. C. Thompson, C. Bonifazi, B. E. Gilchrist, S. D. Williams, W. J. Raitt, J.-P. Lebreton, W. J. Burke, N. H. Stone, and K. H. Wright, "The current-voltage characteristics of a large probe in low earth orbit: TSS-1r results," *Geophysical Research Letters*, vol. 25, no. 4, pp. 413–416, Feb 1998.

[25] M. Cosmo and E. Lorenzini, Eds., *Tethers in Space Handbook*, 3rd ed. Smithsonian Astrophysical Observatory, Dec. 1997.

[26] A. K. Misra, "Space tether missions," Aug. 2018, presented at AAS/AIAA Astrodynamics Specialist Conference in Snowbird, UT.

[27] A. Frias, "Modeling and control of spacecraft systems with couple orbital and attitude dynamics," Master's thesis, Ryerson University, 2010.

[28] K. T. Alfriend, S. R. Vadali, P. Gurfil, J. P. How, and L. S. Breger, *Spacecraft Formation Flying*. Butterworth-Heinemann, 2010.

[29] G. Byrne, "Lecture notes in space technology and applications," Naval Postgraduate School, SSAG, Monterey, CA, spring 2018.

[30] H. D. Curtis, *Orbital mechanics for engineering students*, 3rd ed. United Kingdom: Butterworth-Heinemann, 2014.

[31] R. R. Bates, D. D. Mueller, and J. E. White, *Fundamentals of Astrodynamics*. New York, NY: Dover Publications, Inc., 1971.

[32] H. Schaub and J. L. Junkins, *Analytical mechanics of space systems*, J. A. Schetz, Ed. American Institute of Aeronautics and Astronautics, 2003.

[33] K. Yamanaka and F. Ankersen, "New state transition matrix for relative motion on an arbitrary elliptical orbit," *Journal of guidance, control, and dynamics*, 2002.

[34] Semi-analytic Tool for End of Life Analysis, version 3.2. National Centre for Space Studies (CNES). [Online]. Available: https://logiciels.cnes.fr/en/content/stela

[35] ESA, "Hubble Space Telescope fact sheet," accessed: 2018-10-01. Available: https://www.spacetelescope.org/about/general/fact_sheet/

[36] R. Smith, K. Bledsoe, J. Dobarco-Otero, W. Rochelle, N. Johnson, A. Pergosky, and M. Weiss, "Reentry survivability analysis of the Hubble Space Telescope (HST)," in *Proceedings of the 4th European Conference on Space Debris*, 2005.

[37] Department of Defense, "Space support instruction (DoD Instruction 3100.12)," Sep. 2000.

[38] S. Tragesser, "Formation flying with tethered spacecraft," in *Astrodynamics Specialist Conference*. American Institute of Aeronautics and Astronautics, Aug 2000.

[39] S. G. Tragesser, "Static formations using momentum exchange between satellites," *Journal of Guidance, Control, and Dynamics*, vol. 32, no. 4, pp. 1277–1286, Jul 2009.

[40] K. D. Kumar, T. Yasaka, and T. Sasaki, "Orbit transfer of service vehicle/payload through tether retrieval," *Acta Astronautica*, vol. 54, no. 9, pp. 687–698, may 2004.

[41] J. R. Wertz, D. F. Everett, and J. J. Puschell, Eds., *Space mission engineering: The new SMAD*. Space Technology Library, 2015, ch. Orbits and astrodynamics, p. 232.

[42] Z. Asher, S. Tragesser, C. Kneubel, J. Hudson, T. Bradley, and I. Kolmanovsky, "Space debris field removal using tether momentum exchange." AAS/AIAA, Sep. 2018, presented at 28th Astrodynamics Specialist Conference.

[43] B. Wie, *Space vehicle dynamics and control (AIAA Education Series)*. American Instititute of Aeronautics and Astronautics, 1998.

[44] M. Romano, "Lecture notes in spacecraft disturbance torques," Naval Postgraduate School, MAE, Monterey, CA, spring 2017.

[45] S. Stirone. "This is where the international space station will go to die". Popular Science. [Online]. Available: https://www.popsci.com/this-is-where-international-space-station-will-go-to-die

[46] *Space Vehicle Systems Engineering Handbook*, The Aerospace Corporation, El Segundo, CA, USA, 2006.

[47] I. M. Ross, Q. Gong, M. Karpenko, and R. J. Proulx, "Scaling and balancing for high-performance computation of optimal controls," *Journal of Guidance, Control, and Dynamics*, vol. 41, no. 10, pp. 2086–2097, oct 2018.

[48] I. M. Ross, *A Primer on Pontryagin's Principle in Optimal Control: Second Edition*, 2nd ed. Collegiate Publishers, 2015.

[49] R. Saynak and A. K. Misra, "Frequencies of oscillations of a tether towing space debris." Snowbird, UT: AAS Astrodynamics Specialist Conference, Aug. 2018.

[50] Z. Dang, "Solutions of Tschauner-Hempel equations," *Journal of Guidance, Control, and Dynamics*, vol. 40, no. 11, pp. 2956–2960, Nov 2017.

Initial Distribution List

1. Defense Technical Information Center
   Ft. Belvoir, Virginia

2. Dudley Knox Library
   Naval Postgraduate School
   Monterey, California